Molecular Cancer

RESEARCH Open Access

DCLK1-mediated regulation of invadopodia dynamics and matrix metalloproteinase trafficking drives invasive progression in head and neck squamous cell carcinoma

Levi Arnold[1,2], Marrion Yap[1], Nathan Farrokhian[1], Laura Jackson[1], Michael Barry[1], Thuc Ly[2], Pachiappan Arjunan[1], Angela Kaczorowski-Worthley[1], Carter Tews[1], Avisha Pandey[1], Austin Morrison[2], Michael P. Washburn[2], David Standing[2], Juan P. Gomez[1], Nanda Kumar Yellapu[3], David Johnson[4], Linheng Li[5], Shahid Umar[6], Shrikant Anant[2] and Sufi Mary Thomas[1,2*]

Abstract

Background HNSCC presents a significant health challenge due to its high mortality resulting from treatment resistance and locoregional invasion into critical structures in the head and neck region. Understanding the invasion mechanisms of HNSCC has the potential to guide targeted therapies, improving patient survival. Previously, we demonstrated the involvement of doublecortin like kinase 1 (DCLK1) in regulating HNSCC cell invasion. Here, we investigated the hypothesis that DCLK1 modulates proteins within invadopodia, specialized subcellular protrusions that secrete matrix metalloproteinases to degrade the ECM.

Methods We employed tandem mass tag (TMT)-based proteomics to identify the role of DCLK1 in regulating proteins involved in HNSCC invasion and validated the findings using immunoblotting. The Cancer Genome Atlas (TCGA) database was interrogated to correlate DCLK1 expression with tumor stage, grade, and invasion-associated proteins. In vitro invasion was assessed using a Boyden chamber assay, and immunohistochemistry on patient samples determined DCLK1's distribution within tumors. Gelatin invadopodia assay was used to establish DCLK1 localization to invadopodia related gelatin degradation. Super-resolution confocal microscopy demonstrated colocalization of DCLK1 with invadopodia markers and MMP trafficking proteins. ECM degradation by MMPs in HNSCC cells with wild-type and knockdown DCLK1 was evaluated using a dye-quenched tracer, while gel zymography and MMP array identified secreted proteases. Proximity ligation assay (PLA) and co-immunoprecipitation assays were used to confirm interactions between DCLK1, MMP9, KIF16B, and RAB40B.

Results Proteomic analysis demonstrate DCLK1's role in regulating proteins involved in cytoskeletal and ECM remodeling. Clinically, rising DCLK1 levels correlate with higher histological grade and lymph node metastasis, with heightened expression observed at the leading edge of HNSCC patient tissue. DCLK1 is localized with markers of mature invadopodia including TKS4, TKS5, cortactin, and MT1-MMP. Knockdown of DCLK1 led to reductions in invadopodia numbers and decreased in vitro invasion and ECM degradation. MMP9 colocalizes with DCLK1 within invadopodia structures and its secretion is disrupted by DCLK1 knockdown. Further, PLA and co-immunoprecipitations

*Correspondence:
Sufi Mary Thomas
sthomas7@kumc.edu
Full list of author information is available at the end of the article

studies demonstrate DLCK1 complexes with KIF16B and RAB40B enabling trafficking of degradative MMP9 cargo along the invadopodia to degrade local ECM.

Conclusion This work unveils a novel function of DCLK1 in regulating KIF16B and RAB40B to traffic matrix degrading MMP9 cargo to the distal end of the invadopodia facilitating HNSCC invasion.

Keywords Doublecortin-like kinase 1, HNSCC, Invadopodia, Loco-regional invasion, Tumor microenvironment

Background

Head and neck squamous cell carcinoma (HNSCC) poses a significant global health challenge due to its high incidence rates and adverse effects on patient survival [1]. A key feature of this malignancy is its propensity for locoregional invasion, which greatly contributes to patient mortality and treatment-related complications [2]. The tumor cells' ability to breach local extracellular matrix (ECM) barriers, invading critical structures such as the carotid artery or metastasizing to distant sites contributes to mortality [3]. Understanding these early metastatic events is crucial for shedding light on HNSCC pathogenesis and identifying potential therapeutic targets in a largely underexplored aspect of HNSCC research.

Invadopodia, actin-rich, finger-like cellular projections, play a pivotal role in cancer cell invasion by puncturing the ECM through the secretion of MMPs [4, 5]. Invadopodia formation involves three stages: initiation, assembly, and maturation [6]. Initiation, stimulated by growth factors or other signals, involves the rapid recruitment of key molecular components, that polymerizes actin filaments near the plasma membrane [7]. In the assembly phase, RGD-binding integrins, integrin-linked kinase, vinculin and paxillin create an adhesion ring around the invadopodia [8]. During the maturation phase, cofilin-driven actin polymerization and Arp2/3-dependent actin nucleation facilitate the development of fully functional invadopodia [9]. Importantly, microtubules elongate into invadopodia, providing structural rigidity and serving as a tract for trafficking vesicles containing MMPs [10]. Additionally, emerging research highlights the localization of adaptor protein, tyrosine kinase substrate with four Src homology 3 domains 4 (TKS4) and recruitment of MT1-MMP to the distal end of the invadopodia [11, 12]. Adaptor protein TKS5, acts as a tether for RAB40B that binds to vesicles containing MMPs and transports them to the elongating invadopodia [13]. The development of invadopodia and molecular mechanisms regulating its invasive phenotype are not fully characterized.

Doublecortin like kinase 1 (DCLK1), originally characterized as a microtubule-binding protein, has predominantly been associated with cancer stem cell properties, particularly in colorectal cancer [14]. We recently reported that genetically attenuating DCLK1 or targeting it with a small molecule inhibitor, DiFiD, reduces the ability of HNSCC to degrade and invade through the ECM [15]. Notably, DCLK1's history extends beyond cancer studies and finds its origins in neurobiology. Early research identified DCLK1's presence at the growth cones of axons, where it plays a pivotal role in neural elongation [16]. Studies by Lipka et al. further elaborated on DCLK1's function in the transportation of dense core vesicles, notably in collaboration with the kinesin superfamily, particularly members of the Kinesin 3 family [17].

In our current research, we aimed to unravel the role of DCLK1 in tumor cell invasion, employing proteomic analysis. Our investigations unveiled that DCLK1 exerts significant influence over proteins involved in cell-ECM interactions, cell movement, and cell invasion. Furthermore, our findings demonstrate that DCLK1 forms complexes with KIF16B and RAB40. These complexes facilitate the trafficking of ECM degradative cargo to the distal aspect of invadopodia. Crucially, our research demonstrates that the abrogation of DCLK1 results in a reduction in the secretion of matrix metalloproteases by HNSCC cells. These findings reveal the pivotal role of DCLK1 in cancer invasion and enhance our understanding of invadopodia and HNSCC locoregional invasion.

Results

In the context of HNSCC, the impact of DCLK1 on proteins regulating tumor invasion remains a subject that lacks comprehensive understanding. To address this knowledge gap, we generated shRNA-mediated near complete knockdown of DCLK1 compared to control cells in the FaDu cell line (Fig. 1A). FaDu, is a well-characterized invasive HNSCC cell line with a p53 mutation common in ~ 70% of HNSCC cases, and ideal growth parameters for scaling up cell numbers was chosen for these studies [18]. Five biological replicates of shControl and shDCLK1 cells were then subjected to tandem mass tag spectrometry. The log fold change analysis of DCLK1 knockdown vs control cells were assessed in 6474 proteins and 8477 phospho proteins (Sup. Table 1). The proteomic and phosphoproteomic signatures displayed distinct clustering patterns, highlighting substantial differences in the molecular profiles regulated by DCLK1 (Sup. Figure 1A, B). Between the shControl cells and

the DCLK1 knockdown cells, we identified a substantial alteration in protein expression. While 376 proteins were downregulated in the DCLK1 knockdown cells when compared to the controls, 359 proteins showed upregulation (Fig. 1B). Network ontological analysis of DCLK1-enriched proteins revealed specific interactions related to cell-ECM interaction (Fig. 1C). Hierarchical analysis further identified terms associated with ECM interactions, cytoskeleton reorganization, and cell adhesion (Fig. 1D and E). To understand the functional implications of the identified proteomic and phosphoproteomic alterations, we conducted further analysis using the Metascape tool [19]. The results unveiled a diverse array of roles for DCLK1 in various cellular processes. Notably, there was an enrichment of proteins involved in membrane interactions, particularly in the context of trafficking, suggesting DCLK1's involvement in regulating the transport of cellular components across membranes (Sup. Figure 2A, Sup. Table 2). The data also showed that DCLK1 may be involved in cytoskeletal rearrangement as evidenced by increased expression of associated proteins such as caveolin 3 (CAVIN3), caveolin 1 (CAV1), vimentin (VIM), cortactin (CTTN), cofilin 1 (CFL1), and Actinin Alpha 4 (ACTN4) (Sup. Tables 1, 2). Gene Ontology analysis derived from phospho-kinase profiles (normalized to the respective total proteins levels) demonstrated a high prevalence of proteins involved with cell junctions, actin filament assembly, microtubules and actin crosslink formation in cells expressing DCLK1 compared to cells with knockdown DCLK1 (Sup. Figure 2B). Moreover, these data suggest that DCLK1 contributes to the enhanced motility of tumor cells. To further understand the biological functions regulated by DCLK1, we conducted specific gene ontology studies using the Database for Annotation, Visualization, and Integrated Discovery (DAVID) Bioinformatics tool [20]. We demonstrate that the categorical term "cell projection" is significantly upregulated in DCLK1 control cells compared to DCLK1 knockdown cells. This integrative analysis on phospho and total proteins in the DCLK1 control and knockdown cells highlights the relationship between DCLK1 knockdown and invadopodia and metastasis-associated genes (Sup. Table 1). The analysis revealed that the most significant cluster of terms was related to cellular projections and growth cones (Sup. Figure 2C). These findings further emphasize the role of DCLK1 in regulating cytoskeletal dynamics and enhancing the invasive potential of tumor cells.

Building on this understanding, we sought to determine the broader functional significance of DCLK1-mediated proteomic and phosphoproteomic changes by conducting further integrative analysis. Specifically, we aimed to identify the regulatory kinases that could be driving these DCLK1-dependent processes. To achieve this, we utilized curated libraries like BioGRID [21], MINT [22], STRING [23], and others, facilitated by the KEA3 web tool [24]. Notably, the analysis revealed reduction in the levels of several kinases in the DCLK1 knockdown cells, including Src kinase, epidermal growth factor receptor (EGFR), and P21 (RAC1)-activated kinase 1 (PAK1), aligning with our earlier gene ontology analysis emphasizing roles in locomotion and cytoskeletal rearrangement (Sup. Figure 3A, Sup. Table 3).

Given the complexity of the human kinome, which comprises over 500 kinases grouped into distinct superfamilies, we utilized Coral, a quantitative kinase visualization tool, to better understand the effects of DCLK1 knockdown [25]. This analysis revealed significant downregulation of various kinases, with EGFR emerging as a prominently affected kinase in DCLK1 knockdown cells. Additionally, the CAMK kinase family showed a notable susceptibility to DCLK1 downmodulation, underscoring DCLK1's significant role within this kinase family (Sup. Figure 3B). We validated these findings using immunoblotting to demonstrate decreased EGFR expression on DCLK1 knockdown across three HNSCC cell lines (FaDu, UMSCC1, and CAL33) (Sup. Figure 4A). Furthermore, analysis of patient mRNA data revealed an increasingly positive correlation between DCLK1 expression and EGFR levels across tumor stages, underscoring the potential clinical relevance of DCLK1 in regulating key pathways involved in tumor progression (Sup. Figure 4B).

Given that phosphorylation is a key post-translational modification that regulates a wide array of cellular processes, including signal transduction, cytoskeletal dynamics, and cellular motility, we next

(See figure on next page.)

Fig. 1 DCLK1 knockdown regulates expression of several genes. **A** Immunoblot analysis of DCLK1 knockdown in HNSCC FaDu cells is presented, with five independent experimental replicates confirming consistent reduction in DCLK1 levels compared to the control. Actin was used as a loading control to ensure equal protein loading across all lanes. **B** A volcano plot is provided, depicting proteins that are either downregulated (in red) or upregulated (in blue) in shDCLK1 cells relative to the control, with log2 fold change greater or less than 1.0. Functional annotation of DCLK1 is detailed, including gene ontology enrichment analysis of (**C**) pathway network enrichment, (**D**) biological processes, and (**E**) hierarchical dendrogram. Fisher's exact test was employed for the functional annotation, with a significance threshold of P-value < 0.05 determined using the Benjamini–Hochberg procedure to identify statistically significant values. The figures were generated using ShinyGO

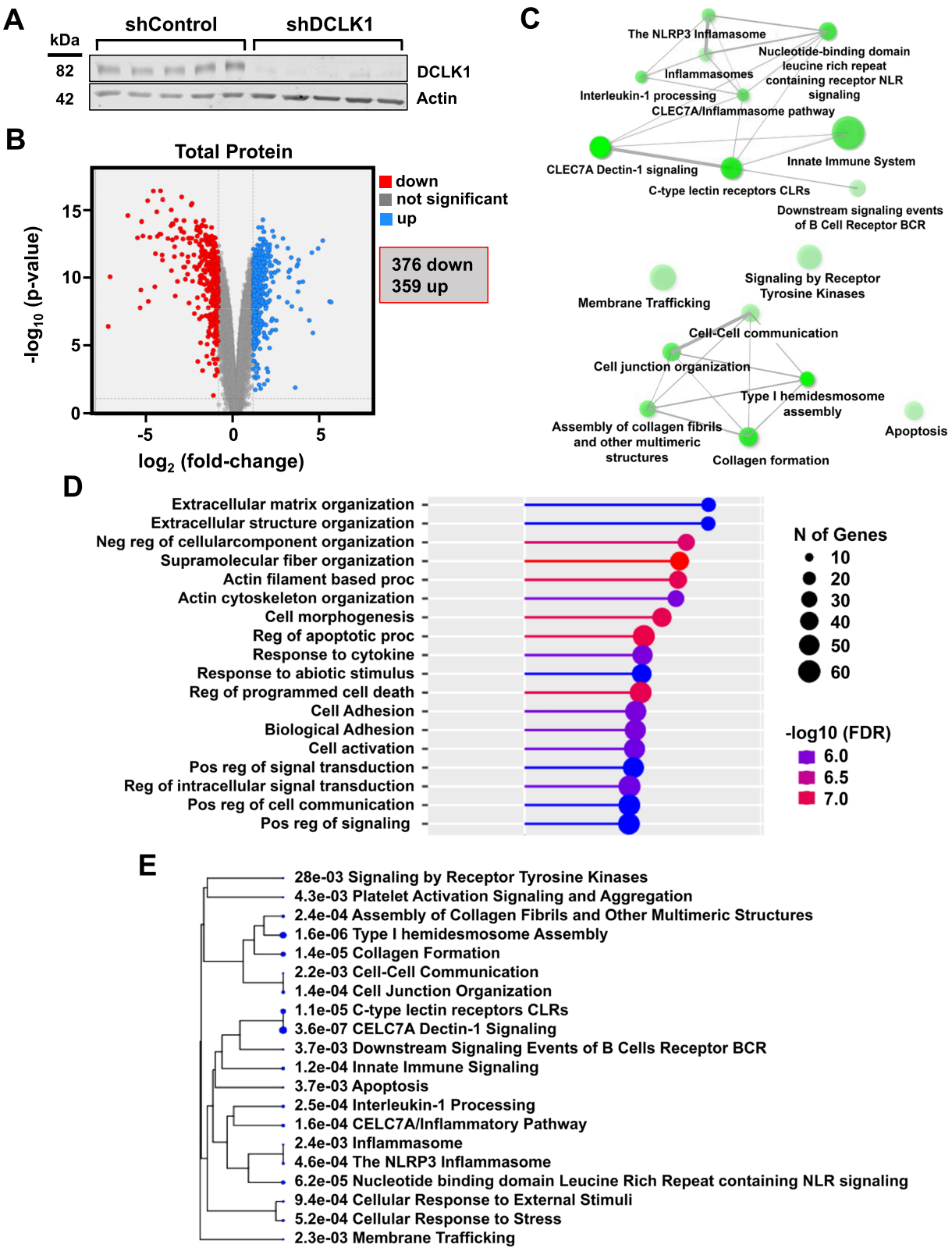

Fig. 1 (See legend on previous page.)

turned our attention to the phosphoproteome to better understand DCLK1's broader impact. Our phosphoproteomic analysis revealed significant differences in phosphorylation patterns, with 824 unique phosphopeptides exhibiting higher levels in DCLK1 knockdown cells compared to controls, while 1,249 unique phosphopeptides were significantly reduced (Fig. 2A, Sup. Table 1). To further clarify the functional implications of these phosphorylation changes, we examined kinase activity associated with DCLK1 using the RoKAI/RoKAI Explorer tool [26]. Additionally, functional ontology analysis based on the comparison of total phosphopeptides to total peptides identified key biological processes linked to cytoskeletal rearrangement and movement, particularly involving actin filaments and microtubules. This analysis also highlighted significant enrichment of terms associated with membrane interactions, including plasma membrane localization, cell junctions, and focal adhesion in DCLK1-enriched samples (Fig. 2B). These findings strongly suggest that DCLK1 plays a crucial role in regulating cellular motility, invasion, and cytoskeletal interactions. Further analysis of individual kinase activity revealed significant associations between DCLK1 and key kinases, including EGFR, ERK1/2, Src, and PAK1 (Fig. 2C, Sup. Table 4). Together, these insights provide a more comprehensive understanding of DCLK1's influence on essential cellular functions, particularly its regulatory role in pathways governing cell invasion. Together, these insights provide a more comprehensive understanding of DCLK1's influence on essential cellular functions, particularly its regulatory role in pathways governing cell invasion.

DCLK1 localizes to HNSCC invadopodia, driving cellular invasion

Unfavorable outcomes in HNSCC patients are often associated with locoregional invasion, a less explored aspect of the disease. Our previous work demonstrated that DCLK1 knockdown reduces cell invasion [15]. Analysis of The Cancer Genome Atlas (TCGA) data revealed a significant correlation between DCLK1 expression and advanced HNSCC, particularly in relation to higher lymph node staging and tumor histologic grade (Fig. 3A and B).

Further investigation using immunohistochemical (IHC) analysis of specimens from HNSCC patients ($n=40$) revealed that DCLK1 expression is markedly elevated in poorly differentiated tumor cells at the invasive boundary, where the tumor interacts with the surrounding stroma (Fig. 3C). We observe that the well-differentiated regions of the tumor have low expression of DCLK1. Quantification of DCLK1 staining from the differentiated core of the tumor to the leading edge with poorly differentiated SCC clearly demonstrates a higher intensity of staining close to the edge of the tumor (Sup. Figure 5A). In contrast, normal oral mucosa exhibited little to no DCLK1 expression (Sup. Figure 5B). Notably, DCLK1 expression was observed in collective invasive strands (blue arrow), detached groups (red arrow) and individual tumor cells (black arrow) (Sup. Figure 5C).

Given DCLK1's known function in trafficking proteins within neuronal cells, we hypothesized that DCLK1 could similarly facilitate HNSCC invasion by transporting MMP cargo to the distal ends of lengthening invadopodia. Invadopodia are crucial for initiating ECM degradation, thereby allowing tumor cells to penetrate the surrounding matrix. There are no molecular markers that define cell protrusions including filopodia and invadopodia. However, invadopodia are characterized by ECM degradation accompanying cancer cell invasion [27]. Cellular protrusions seen in non-cancer with similar structure and function are called podosomes. The degradative activity of invadopodia distinguish them from other cell protrusions with adhesive properties like focal adhesions, lamellipodia or filopodia [28].

To confirm DCLK1's role in invadopodia function, the small molecule inhibitor DiFiD, which effectively binds to and inhibits DCLK1 kinase activity [15], was utilized alongside a well-established conventional 2D gelatin invadopodia assay commonly employed in the field (schematic in Sup. Figure 5D) [29, 30]. HNSCC cells plated on FITC labeled gelatin displayed invadopodia, with DCLK1 localizing with actin in areas of gelatin degradation under DMSO control conditions. In contrast, treatment with 10 nM DiFiD resulted in a reduction of gelatin degradation, and the localization of DCLK1 with actin

(See figure on next page.)

Fig. 2 DCLK1 regulates the phosphoproteome. **A** A volcano plot is provided, depicting phosphopeptides that are either downregulated (in red) or upregulated (in blue) in shDCLK1 cells relative to the control, with log2 fold change greater or less than 1.0 in FaDu cells. **B** The volcano plot showcases the outcomes of Gene Ontology analysis derived from inferred phospho-kinase analysis of phosphopeptides using the RoKAI Explorer web tool [26]. The dashed line indicates the significance threshold, with significant Gene Ontology terms highlighted in red and insignificant terms in blue. The maximum false discovery rate is set at 0.05, and the minimum absolute log2-fold change is set at 1.0. **C** The bar chart represents inferred phospho-kinase activity generated through the RoKAI web tool [26]. Each bar's color corresponds to the z-score level of the kinase, with red indicating a higher score and blue indicating a lower score. Activity levels are determined based on the log2-fold change of phosphopeptides that are differentially expressed between shControl cells and shDCLK1 cells

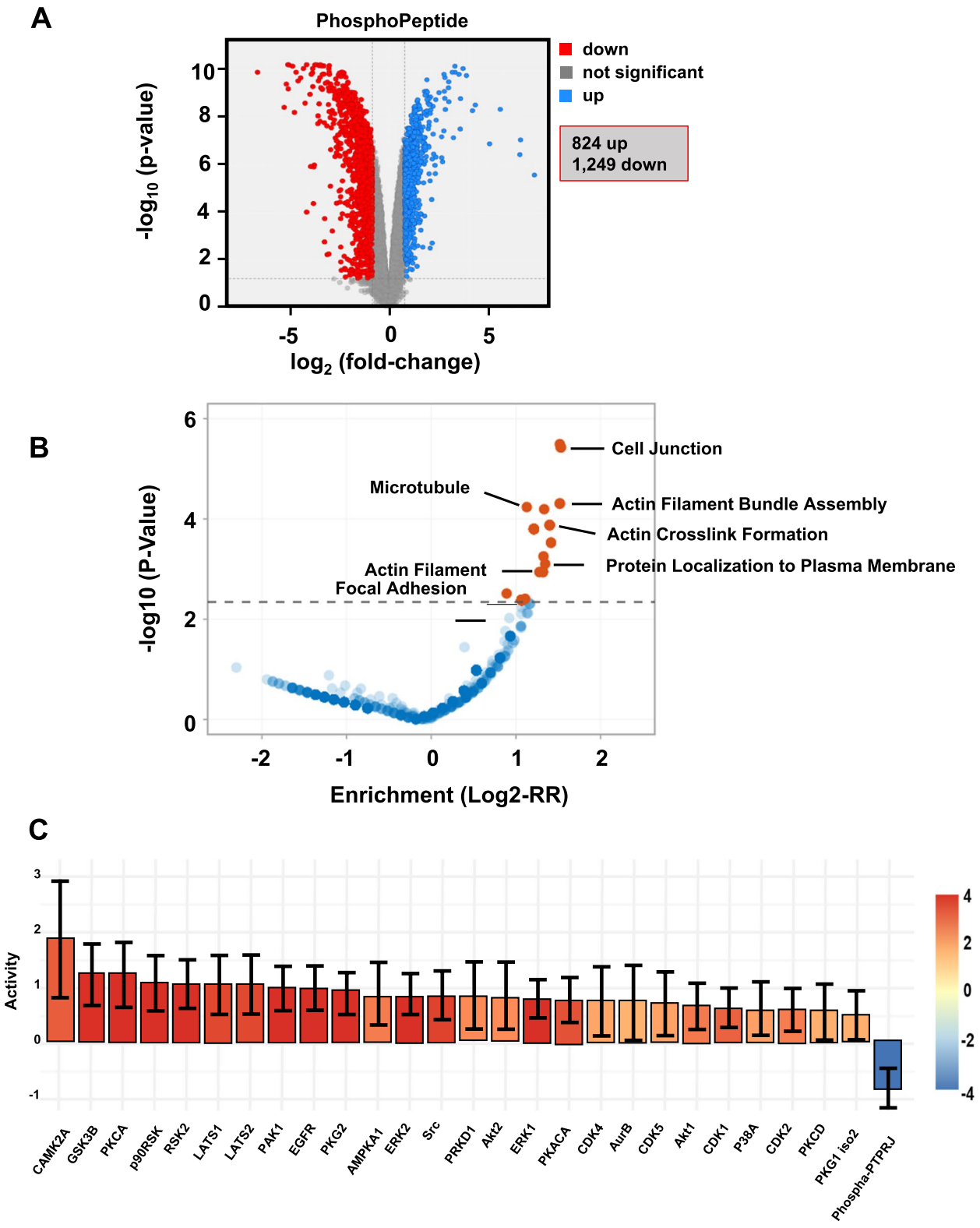

Fig. 2 (See legend on previous page.)

within invadopodia was also diminished (Fig. 3D, Sup. Figure 5E, F).

In addition to the conventional 2D assay, we also tested invadopodia formation in a 3D assay. To better approximate the spatial constraints and ECM interactions of HNSCC cells within a 3D environment, a base layer of VitroGel, a well-defined hydrogel that closely mimics the extracellular environment, was laid down [31]. HNSCC cells, suspended in VitroGel, were then seeded onto this base layer, forming a thin, uniform layer that facilitated predictable localization of the cells after polymerization. This setup allowed the cells to be seeded precisely within a single plane to facilitate imaging. After allowing the cell-laden VitroGel layer to polymerize, an additional layer of VitroGel was applied over the cells (schematic in Sup. Figure 5G). This structure was designed to maintain cell viability while also providing a controlled environment for studying invasive behavior and matrix interactions [32–37]. Additionally, we performed comparative analyses to validate the effectiveness of VitroGel using the traditional 2D invadopodia assay, comparing it against gelatin and Matrigel matrices. These assays demonstrated that HNSCC cells exhibited similar patterns of focal degradation across all tested matrices, with DCLK1 and actin prominently co-localizing at the degradation sites (Sup. Figure 5H, 5I, 5J).

Because DCLK1 modulation can influence cell proliferation, we evaluated its effect on invadopodia formation in under 12 h. With FaDu cells having a doubling time of 48 h, we fixed and assessed the cells using microscopy within 12 h post-seeding. Our results revealed a significant reduction in the number of cellular projections (pseudo colored in red) in DCLK1 knockdown cells compared to wild-type controls (Fig. 3E).

To confirm the role of DCLK1 in invadopodia formation, we evaluated its localization within the cell using super-resolution microscopy. The data demonstrate that DCLK1 (green) localizes to HNSCC invadopodia (Fig. 3F). Additionally, we observed filamentous actin (F-actin, red) localization, consistent with established knowledge of the actin-rich nature of invadopodia [38]. Importantly, the localization patterns of DCLK1 and actin within invadopodia were not extensively overlapping (Fig. 3F insets). The observed elongated, linear patterns of DCLK1, protruding parallel to cellular extensions, indicate that the localization of DCLK1 to invadopodia is not contingent upon actin-DCLK1 co-localization.

Invadopodia are the functional cellular units of invasive tumor cells; so, we conducted a transwell Boyden chamber experiment to assess the impact of DCLK1 on the invasive potential of HNSCC cells. In this experiment, HNSCC cells were seeded onto a VitroGel substrate in the upper chamber and allowed to invade through the substrate towards the lower chamber. Our findings demonstrated that DCLK1 knockdown resulted in a significant reduction in the number of cells capable of effectively penetrating the gel and traversing to the lower chamber ($p=0.014$). (Fig. 3G).

To establish DCLK1 as a bona fide component of invadopodia, we conducted co-immunofluorescence studies with DCLK1 and TKS4, TKS5, cortactin, or MMP14 (also called MT1-MMP) which are well characterized markers of mature invadopodia [39–42]. The analysis revealed significant colocalization between DCLK1 and TKS4, an adapter protein predominantly present in mature invadopodia (Fig. 3H). Additionally, DCLK1 exhibited colocalization with TKS5, an adapter protein involved MMP transport (Fig. 3I). FaDu cells have an amplification on chromosome 11q13, a region amplified in nearly 25% of all HNSCC patients, that carries the cortactin gene. The cells exhibit elevated levels of cortactin (COSMIC database, data not shown). However, despite the increased levels of cortactin in FaDu cells, it colocalizes with DCLK1 in invadopodia of HNSCC (Fig. 3J). Lastly, DCLK1 and MMP14, a membrane-bound metalloprotease responsible for ECM degradation, were both seen in invadopodia (Fig. 3K). Quantitative analysis of protein colocalization was performed on the confocal microscopy images from Fig. 3G-J as previously described [43].

(See figure on next page.)

Fig. 3 DCLK1 promotes HNSCC cellular invasion. Clinical data from TCGA reveal heightened DCLK1 expression in (**A**) progressed lymph node stage, and (**B**) escalating histologic grade of head and neck squamous cell carcinoma (HNSCC). **C** Representative immunohistochemistry (IHC) staining of a HNSCC patient sample depicts elevated DCLK1 staining at the tumor-stroma interface (400X magnification, $n=40$). **D** Confocal images alongside orthogonal sectioning of FaDu cells captured using a 100× oil immersion objective demonstrate colocalization of DCLK1 (cyan) with actin (magenta) at sites of FITC-labeled gelatin degradation (grayscale). Red arrowheads denote areas of gelatin degradation. Comparison images show FaDu cells pretreated with 10 nM DiFiD for 2 h, highlighting differences in DCLK1 and actin localization. **E** Invadopodia (pseudo colored red, black arrows) in shControl and DCLK1 knockdown cells. Box and whisker plot quantifies invadopodia in 5×10^3 cells across three replicate experiments using ImageJ. **F** Confocal images illustrate DCLK1 (green) and F-actin (red) colocalization in invadopodia of FaDu cells. Images captured using a 40X oil immersion lens objective. **G** HNSCC cell invasion across the Boyden chamber, normalized to cell viability. Error bars indicate ± SEM. Confocal imaging of DCLK1 (green) with invadopodia markers (red) and DAPI reveals colocalization of DCLK1 with (**H**) TKS4, (**I**) TKS5, (**J**) cortactin, and (**K**) MMP14. Oil immersion at 100× objective

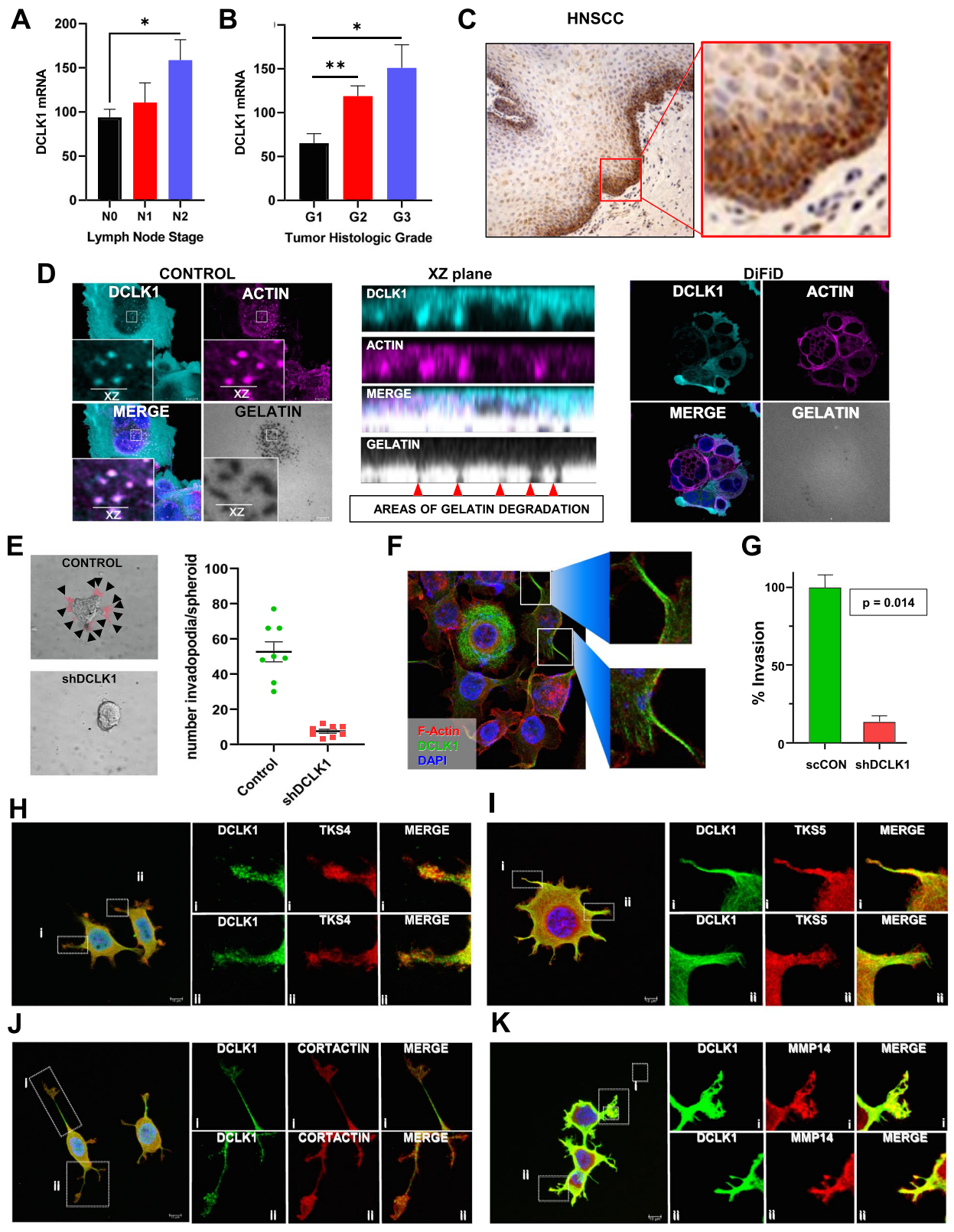

Fig. 3 (See legend on previous page.)

Manders coefficients, which quantify the degree of colocalization between two fluorescent signals by measuring the proportion of one signal that overlaps with the other, were used to assess DCLK1's spatial association with invadopodia markers. The colocalization analysis of DCLK1 with individual invadopodia markers TKS4, TKS5, cortactin, or MMP14 revealed a pronounced decrease in colocalization as the distance from the invadopodia edge increased (Sup. Figure 6A). Aggregated data showed Manders coefficients (tM1 and tM2) and Pearson's correlation for DCLK1 colocalization with all these markers together, further indicating a significant reduction in colocalization with increasing edge distance (Sup Fig. 6B). Quantification of cortactin immunofluorescence signals from Fig. 3I, demonstrate colocalization of DCLK1 and cortactin are highly correlated and decrease as the distance from the plasma membrane increases (Sup. Figure 6A and B). These data suggest that DCLK1 is primarily localized to the periphery of the cell, where active ECM degradation occurs, and may play a critical role in organizing or maintaining the structural integrity of invadopodia in regions closest to the matrix interface. Supporting this role, DCLK1 knockdown led to a marked reduction in fluorescence within knockout cells, which was accompanied by a corresponding decrease in the levels of TKS4, TKS5, cortactin, and MMP14 (Sup. Figure 6C, D, E). We noted that knockdown of DCLK1 did not significantly modulate cortactin levels. However, DCLK1 knockdown reduced its colocalization signal with cortactin. The Pearson correlation score for DCLK1-cortactin changed from 0.605 in control FaDu cells to 0.351 in DCLK1 knockdown, and 0.776 in control UMSCC1 cells to 0.392 in DCLK1 knockdown (Sup. Figure 6E). To validate these findings, we revisited the conventional 2D invadopodia assay, comparing the localization patterns observed in the 3D assay setup. The 2D invadopodia assay confirmed that DCLK1 colocalizes with TKS4, TKS5, cortactin, and MMP14, mirroring the colocalization patterns seen in the 3D assay (Sup. Figure 6F - 6I). This consistency across different assay formats supports the observation of DCLK1's colocalization with invadopodia markers under varied experimental conditions.

Additionally, we performed expression analysis of patient mRNA and protein levels for the selected invadopodia markers, including TKS4, TKS5, cortactin, and MMP14 (Sup. Figure 6J). Proximity ligation assay (PLA) confirmed the close spatial interaction between DCLK1 and TKS4 (Sup. Figure 6K).

DCLK1 regulates the secretion of matrix metalloprotease 9

The degradation of surrounding ECM is an important step in the process of cell invasion. To detect MMP activity at the leading edge of HNSCC spheroids, we utilized a dye-quenched (DQ)-gelatin assay, where the ECM contains quenched FITC-labeled gelatin [44]. Upon gelatinolytic activity, the DQ substrate is cleaved into brightly fluorescent peptides that can be detected using a fluorescence microscope or plate reader. We found that DCLK1 localization correlated with focal areas of gelatin degradation (Sup. Figure 7A-C). To examine the role of DCLK1 in ECM degradation, we used DCLK1 knockdown and control cells. We observed a significant reduction in DQ-saturated VitroGel degradation following DCLK1 knockdown, indicating that DCLK1 plays a critical role in promoting the secretion of metalloproteases (Fig. 4A, Sup. Figure 7D). Additionally, quantification of the signal using a fluorescence plate reader, demonstrated that the knockdown significantly decreased fluorescence intensity over time, with reductions observed at 12, 18, and 24 h, respectively (Sup. Figure 7E). Additionally, cells were treated with the DCLK1 inhibitor DiFiD (10 nM), EGFR inhibitor erlotinib (2 nM), or a combination of both, and degradation activity was quantified using DQ fluorescence intensity (Sup. Figure 4F). ECM degradation was significantly reduced by both erlotinib and DiFiD individually compared to the control, with the combination of both inhibitors producing an additive effect.

To further characterize the MMPs regulated by DCLK1, we evaluated conditioned media (CM) from shControl and DCLK1 knockdown cells using gelatin zymography and an MMP array. We conducted

(See figure on next page.)

Fig. 4 DCLK1 regulates secretion of MMP9 from HNSCC. **A** Representative confocal imaging depicts DCLK1 (red) along with DQ degradation (green) in FaDu cells. Notably, DCLK1 knockdown leads to a marked reduction in DQ gelatin degradation. **B** Gelatin zymography reveals concentrated supernatants from shControl or shDCLK1 cells. White bands against a stained blue background indicate degradation areas, with specific MMPs identified based on their known molecular weights. **C** CM supernatants from shControl or shDCLK1 cells were analyzed using an MMP array. **D** Densitometric quantification of MMP 9, 1 and 13 levels in control and DCLK1 knockdown cells. Error bars represent ± SEM. **E** Confocal imaging of PLA between DCLK1-MMP9 or DCLK1-MMP1 in FaDu HNSCC cells. Images obtained at 40 × oil immersion objective (representative image of 3 biological replicates from FaDu cells. **F** MMP9 ELISA bar graph compares CM from shControl (green) and shDCLK1 (red) under different treatment conditions. Error bars represent ± SEM. ** $P < 0.001$, *** $P < 0.0001$ (**G**) Super resolution confocal microscopy demonstrate DCLK1 (green) and MMP9 (red) (yellow) in FaDu cells. Images on the right are digital magnifications of the inset white box in the 100X oil immersion objective image of FaDu cells

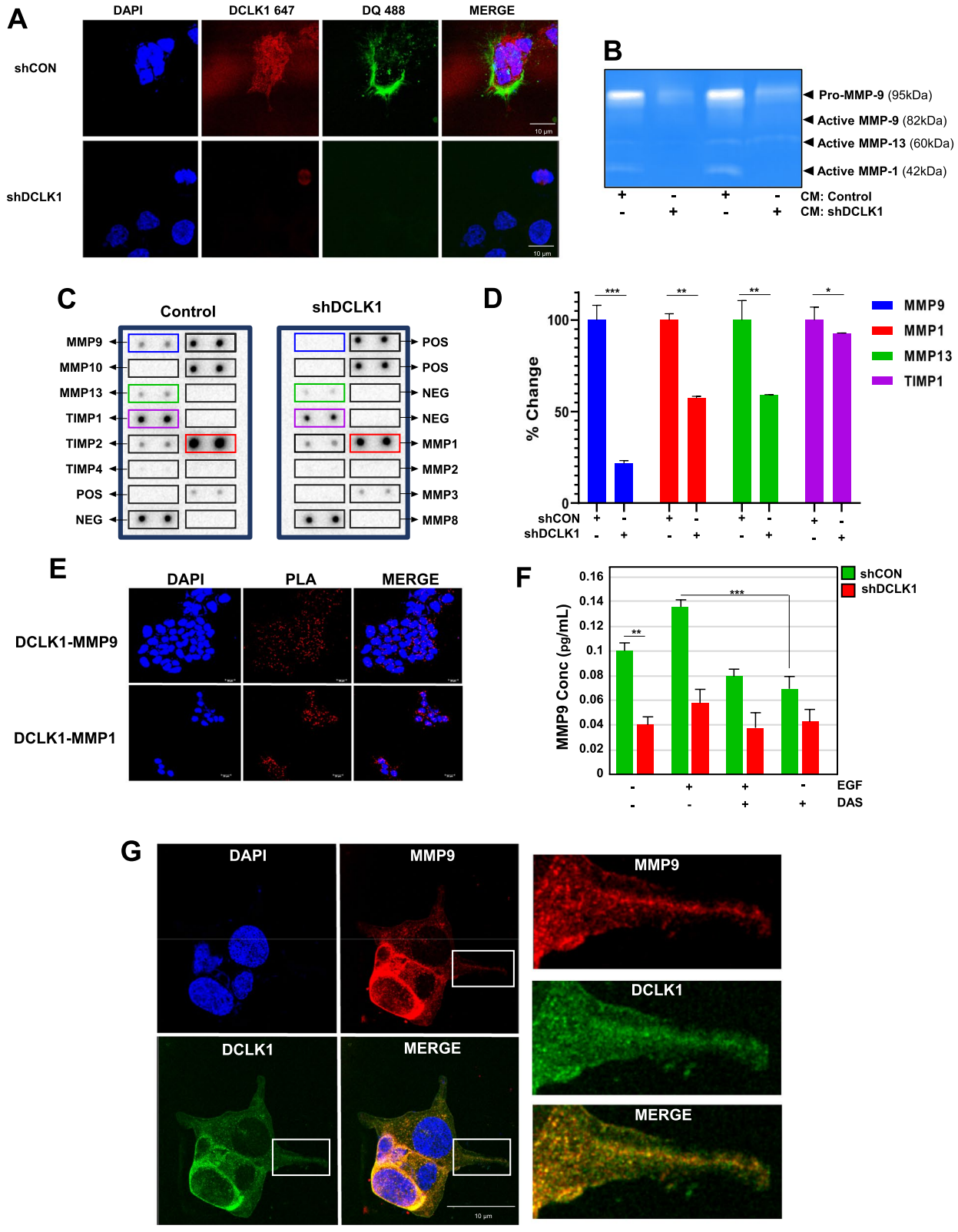

Fig. 4 (See legend on previous page.)

zymography using SDS page gels embedded with gelatin to visualize and quantify enzyme activity in the CM samples. We observed reduced secretion of both pro and active forms of MMP9, active MMP13, and MMP1 (Fig. 4B). Notably, MMP2 secretion was not significantly detected in either the knockdown or control CM samples. Our results confirmed reduced levels of MMP 9, 13 and 1 in CM from DCLK1 knockdown HNSCC (Fig. 4C, D) $p < 0.001$). Interestingly, TIMP1 levels were attenuated on DCLK1 knockdown by 20%. Since this reduction may not be biologically significant, we excluded in from the current investigation. Employing PLA, we demonstrate that DCLK1 was in proximity (< 40 nm) with both MMP9 and MMP1, with a higher frequency of interactions observed between DCLK1 and MMP9 (Fig. 4E). This further demonstrates that DCLK1 associates with MMPs, particularly with MMP9.

EGFR signaling leads to c-Src activation, subsequently promoting actin assembly, polymerization, and cortactin activation, which results in invadopodia formation [45]. We previously reported that inhibition of c-Src attenuates EGFR ligand, EGF induced invasion on HNSCC cells [46, 47]. Dasatinib, a potent Src inhibitor, effectively inhibits Src activity [48]. To examine the impact of DCLK1 knockdown on MMP secretion we analyzed CM from shControl and shDCLK1 HNSCC cells treated with EGF in the presence or absence of dasatinib. To investigate the impact of DCLK1-mediated MMP9 secretion, we conducted an enzyme-linked immunosorbent assay (ELISA) using CM from HNSCC cells. Initially, when HNSCC cells were exposed to EGF, we observed an increase in MMP9 secretion, indicating that EGF promotes MMP9 secretion (Fig. 4F). However, treatment with Src inhibitor, dasatinib resulted in a noticeable reduction in EGF induced MMP9 secretion. DCLK1 knockdown cells had overall lower levels of MMP9 secretion compared to the shControl cells. However, there was a slight though non-significant increase in MMP9 levels on EGF stimulation which came down to baseline levels on dasatinib treatment.

Similarly, gel zymography confirmed an overall decrease in the ability of CM from shDCLK1 cells to degrade gelatin, even after EGF stimulation (Sup. Figure 8A). We also tested the CM from cells that were transiently knocked down with siDCLK1 and observed a similar reduction in MMP secretion (Sup. Figure 8B). When HNSCC cells were pretreated with a low dose of DiFiD (10 nM) we observed reductions in MMP degradation comparable to those seen in dasatinib-treated cells (Sup. Figure 8C). To rule out the possibility that DCLK1 was downregulating cytosolic MMP9 expression, we performed an ELISA on HNSCC cell lysates with and without DCLK1 knockdown and found no significant difference in MMP9 levels (Sup. Figure 8D). Of note, is that the antibody we used could detect the N-terminal of both pro- as well as cleaved MMP9. Additionally, correlation analysis of patient mRNA data revealed a weak relationship between MMP9 and DCLK1 expression ($R = 0.16$, $p < 0.001$) (Sup. Figure 8E). Thus, DCLK1 does not regulate levels of MMP9 total protein but is necessary for the secretion of MMP9 from HNSCC cells.

We sought to determine if DCLK1 actively participated in the intracellular trafficking of MMPs to the distal ends of invadopodia using confocal microscopy. Our findings revealed a clear colocalization between DCLK1 and MMP9 within invadopodia (Fig. 4G). We observed increased MMP9 staining in the cytoplasm and near the plasma membrane in cells lacking invadopodia, a pattern consistent with findings in other studies [49–51]. However, in areas where cells were more spread out, it was evident that DCLK1 and MMP9 specifically overlap within the invadopodia. Notably, DCLK1 displayed well-organized, centrally located extensions that reached towards the distal ends of invadopodia. This spatial arrangement strongly suggests that DCLK1 actively regulates MMP secretion within the context of invadopodia, contributing to their role in promoting the invasive behavior of HNSCC cells. Across all our experimental analyses, including zymography and MMP array assays, we consistently found that DCLK1-mediated MMP secretion did not involve MMP2. To further validate this observation, we performed confocal imaging and co-staining for DCLK1 and MMP2. The results confirmed the findings from the MMP array, showing minimal colocalization between DCLK1 and MMP2 across two HNSCC cell lines (Sup. Figure 8F, G). These findings suggest that DCLK1 primarily interacts with MMP9, rather than MMP2.

DCLK1 regulates the KIF16B motor protein and RAB40B

MMP secretion is a critical function of mature and activated invadopodia [52]. Given that MMPs are transported by motor proteins, our goal was to identify the specific motor proteins interacting with DCLK1. To accomplish this, we conducted an extensive screening of pan-kinesins utilizing TCGA. We observed a strong correlation between DCLK1 and the Kinesin 3 sub-family across all stages of HNSCC (Fig. 5A). Within this group, KIF1B exhibited high levels of correlation with DCLK1, particularly as the tumor stage increased. Additionally, ChipSeq experiments assessed using TNMplot [53] demonstrate correlation of DCLK1 to KIF1A, KIF1B, KIF1C, and KIF16B compared to normal head and neck tissue (Fig. 5B). Likewise, gene expression of the Kinesin-3 family is starkly different from normal, demonstrating a

dramatic increase in KIF1B, KIF1A, KIF14, and especially KIF16B (Fig. 5C).

Next, we utilized the PLA technique to identify the specific members of the Kinesin 3 family that are in proximity with DCLK1. Our results showed that KIF16B but not KIF1A, 1B, 1C and 26B, exhibited a discernible preferential association with DCLK1 in HNSCC cells (Fig. 5D; Sup. Figure 9). Previous reports suggest an interaction between DCLK1 and KIF1A in neuronal cells [17]. However, we observed DCLK1 associates with the Kinesin 3 subfamily, as indicated in the pan-kinesin TCGA screen (Fig. 5A). Using PLA, we demonstrated proximity between DCLK1 and KIF16B, an anterograde kinesin (Fig. 5E, Sup. Figure 10A). Our findings suggest a distinct preference of DCLK1 for binding with KIF16B. Co-immunoprecipitation further confirmed that this interaction is disrupted by DCLK1 inhibitor, DiFiD (Sup. Figure 10B).

To validate the colocalization of DCLK1, TKS4, and KIF16B, we conducted immunofluorescence studies using HNSCC cell lines treated with EGF (5 min), dasatinib (2 h), a combination of dasatinib and EGF, or a DMSO control. Our results demonstrated that EGF stimulation increased the colocalization of DCLK1, KIF16B, and TKS4 (Sup. Figure 11). Conversely, the inhibition of Src using dasatinib disrupted the colocalization with DCLK1.

DCLK1 forms a complex with trafficking proteins KIF16B and RAB40B

Previous reports demonstrate that RAB40B plays a crucial role in regulating the localization of MMP2/9 to invadopodia, and the depletion of RAB40B resulted in decreased cellular degradation and invasion capabilities of breast cancer cells [13, 52]. After confirming the binding interaction between DCLK1 and KIF16B and their potential role in transporting MMP cargo, our next objective was to demonstrate their spatial proximity within HNSCC cells. We performed PLA for DCLK1, KIF16B, and RAB40B, and observed the formation of protein complexes even under control conditions. This interaction was further enhanced following EGF treatment (Fig. 6A, B; Sup. Figure 12A). However, co-treatment with dasatinib significantly suppressed this interaction (Fig. 6A, B). Co-immunoprecipitation further confirmed that DCLK1 interaction with RAB40B is disrupted by DiFiD treatment (Sup. Figure 10B). Confocal imaging further revealed that DCLK1, KIF16B, and RAB40B colocalize within invadopodia (Fig. 6C). The overlap of these proteins within invadopodia suggests their collective involvement in these structures. Knockdown of DCLK1 led to a noticeable reduction in the colocalization of the complex (Fig. 6C, Sup. Figure 13).

Alphafold3 was used to model the DCLK1 kinase domain with KIF16B, ATP, and two Mg+2 ions (ref above). PhosphoSitePlus [54] predicted several residues in the KIF16B motor domain along with S662 and T1024 to be potentially phosphorylated by DCLK (Sup. Figure 14A, B) Therefore, modeling was performed using three KIF16B constructs: the motor domain (residues 3–358) and KIF16B peptides centered on S662 and T1024. Although Alphafold3 was unable to model an interaction that would support phosphorylation of the motor domain, it was able to generate models with the two peptides with high confidence (iptm 0.77 and ptm of 0.87 for the peptide with S662 and iptm 0.8 and ptm 0.89 for the peptide with T1024) (Sup. Figure 14A, B). Furthermore, the targeted serine or threonine was located near the terminal phosphate of ATP. Although we cannot conclude that DCLK1 does not phosphorylate residues in the motor domain, these results support the hypothesis that DCLK1 may act on at least S662 and T1024 of KIF16B.

Alphafold3 was also used to model the DCLK1 kinase domain with RAB40B, ATP, and two Mg^{+2} ions [54]. PhosphoSitePlus [54] predicted two residues in the SOCS box (S224 and S226) domain along with a residue in the disordered C-terminal tail (S247). Therefore, modeling was performed using three constructs: the SOCS box (residues 175–228), the SOCS box with much of the disordered C-terminus (residues 175–260), and the disordered C-terminus (residues 230–278). Both constructs that contained part of the disordered C-terminus generated models that would suggest DCLK1 could phosphorylate a serine in the C-terminus of RAB40B. However, instead of S247, it was S240 that was modeled to be

(See figure on next page.)

Fig. 5 DCLK1 is associated with the kinesin 3 motor protein KIF16B. **A** Heatmap displaying the correlation between DCLK1 and members of the kinesin superfamily across stages 0–3 HNSCC. **B** Correlation matrices from ChIP-seq data illustrate the correlation between DCLK1 and Kinesin 3 family members in normal tissue and HNSCC. **C** Protein expression analysis reveals distinct patterns of Kinesin 3 family members in normal tissue and HNSCC, with the pie size indicating fold change and concentric circles representing varying *p*-value thresholds for statistical significance. **D** Bar graph depicting the results of PLA screen, demonstrating the proximity of DCLK1 to select Kinesin 3 family members. Error bars represent ± SEM. **E** Confocal and brightfield imaging of PLA between DCLK1 and KIF16B in FaDu with red puncta indicating an associated between the two proteins. Images acquired using a 40× oil immersion objective

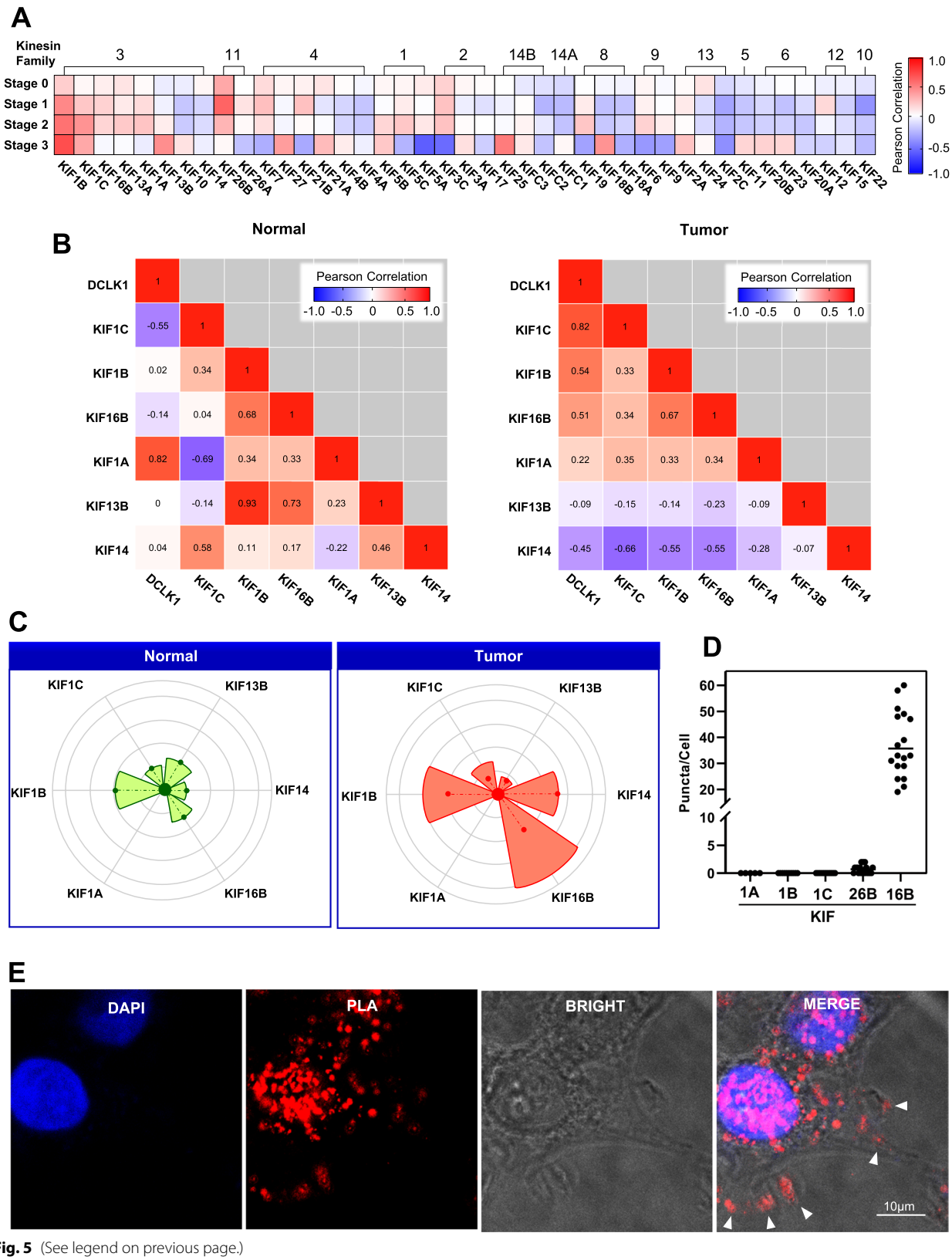

Fig. 5 (See legend on previous page.)

positioned for phosphorylation, with the the C-terminal construct generating a model of high confidence (iptm 0.78 and ptm of 0.85) (Sup. Figure 14C). Although we cannot conclude that DCLK1 does not phosphorylate residues in the SOCS box, this result support the hypothesis that DCLK1 may act on at least S240 of RAB40B.

Discussion

Invadopodia-mediated degradation plays a critical role in promoting locoregional invasion in HNSCC, significantly impacting overall mortality [55]. While extensive research has focused on understanding the activation and initiation of invadopodia, particularly their extracellular to intracellular dynamics, our knowledge of the mature phase of invadopodia, involving microtubule extension and cargo transportation in HNSCC, remains limited [56]. Although it's clear that vesicle transfer occurs along invadopodia in a plus-end direction facilitated by microtubules, investigations into the specific regulatory factors in this process are lacking [52]. In this context, DCLK1 stands out as a compelling candidate due to its potential role as a microtubule binding protein known for participating in cargo transport and driving cancer progression [17].

Previously, DCLK1's role in promoting cancer cell invasion has been predominantly attributed to its facilitation of EMT, with limited attention given to its direct association with the invasion machinery [57]. Earlier studies utilizing Boyden chamber assays focused solely on invasion function, yielding relatively binary results indicating the presence of cells that have invaded through a barrier without elucidating the mechanism of invasion. To address this knowledge gap, our research replicated trans-well experiments and specifically examined the presence of DCLK1 within invadopodia. Invadopodia are specialized structures primarily responsible for secreting degradative proteinases during the mature phase of invadopodia formation [58]. While previous studies on MMP secretion in HNSCC mainly focused on vesicular trafficking, particularly targeting to the plasma membrane, the specific kinesins responsible for MMP trafficking in HNSCC and the role of kinesin binding elements remained unknown [52, 58].

In our investigation, we explored the impact of DCLK1 knockout on MMP secretion in HNSCC CM, with a particular focus on gelatinase MMP9, given its relevance in ECM degradation and overexpression in HNSCC [59]. Intriguingly, we observed a significant reduction in MMP secretion, especially MMP9, in CM from DCLK1 knockout cells. This suggests for the first time, a critical role for DCLK1 within invadopodia in regulating MMP9 secretion. Importantly, we also observed gelatinase activity in DCLK1-mediated secretion, further supporting the connection between DCLK1 and MMP9 in ECM degradation during cellular invasion. On the other hand, MMP2, with its broader functional role, is primarily associated with angiogenesis, a distinct process separate from the ECM degradation orchestrated by invadopodia [60]. In contrast, MMP9 displays exceptional degradative activity against the most prevalent ECM substrates found in HNSCC tumors, such as collagen III, IV, and V [61].

While RAB40B has been linked to the vesicular transport of matrix metalloproteases within invadopodia in breast cancer, the specific mechanism governing its locomotion remains to be elucidated [13, 52]. On the other hand, KIF16B features a highly processive motor domain that allows for rapid movements up to 10 µm [62]. This motor protein is instrumental in recycling MT1-MMP from the plasma membrane, thereby facilitating macrophage invasion [63].

EGFR has high clinical relevance in HNSCC since EGFR inhibitor cetuximab is FDA approved for HNSCC even though the objective response rate is around 10%. EGFR is not the sole regulator of invasion in HNSCC. We previously reported that EGFR and hepatocyte growth factor, regulate HNSCC invasion [46, 64]. Further, hypoxia drives EGFR independent invadopodia formation in HNSCC [65]. Further EGFR inhibition does not sufficiently inhibit MMP activity or invadopodia formation in HNSCC [66]. Thus, it is critical to study effectors downstream of EGFR and other regulators of invasion in HNSCC. Our studies demonstrate on stimulation with EGF, DCLK1 mediates invadopodia formation in HNSCC. Knockdown of DCLK1 resulted in reduced EGFR protein levels as assessed by mass spectrometry and validated through immunoblotting. Our observation

(See figure on next page.)

Fig. 6 DCLK1, KIF16B, and RAB40B form a complex in HNSCC. **A** Quantification of multi-plex PLA (images in Sup. Figure 12) depicting the association of DCLK1 to MMP9, RAB40B, or KIF16B in FaDu, UMSCC1, and CAL33. HNSCC cells treated with vehicle control (blue), EGF (10 ng/ml, green), EGF and dasatinib (100 nM, yellow), or dasatinib alone (red). Error bars indicate ± SEM (* indicates $p < 0.05$). **B** Quantification of three-color PLA (imaging shown in Sup. Figure 12) demonstrating overlap coefficient analysis of DCLK1 and MMP9, RAB40B, or KIF16B under the experimental conditions mentioned in 6A in FaDu, UMSCC1, and CAL33 cells. Error bars represent ± SEM. **C** Confocal microscopy images capturing the localization of DCLK1 (green), RAB40B (red), and KIF16B (white) in invadopodia of FaDu shControl or shDCLK1 cells. Each inset (i, ii) showcases individual cellular projections. Images were obtained using oil immersion at a 100 × objective

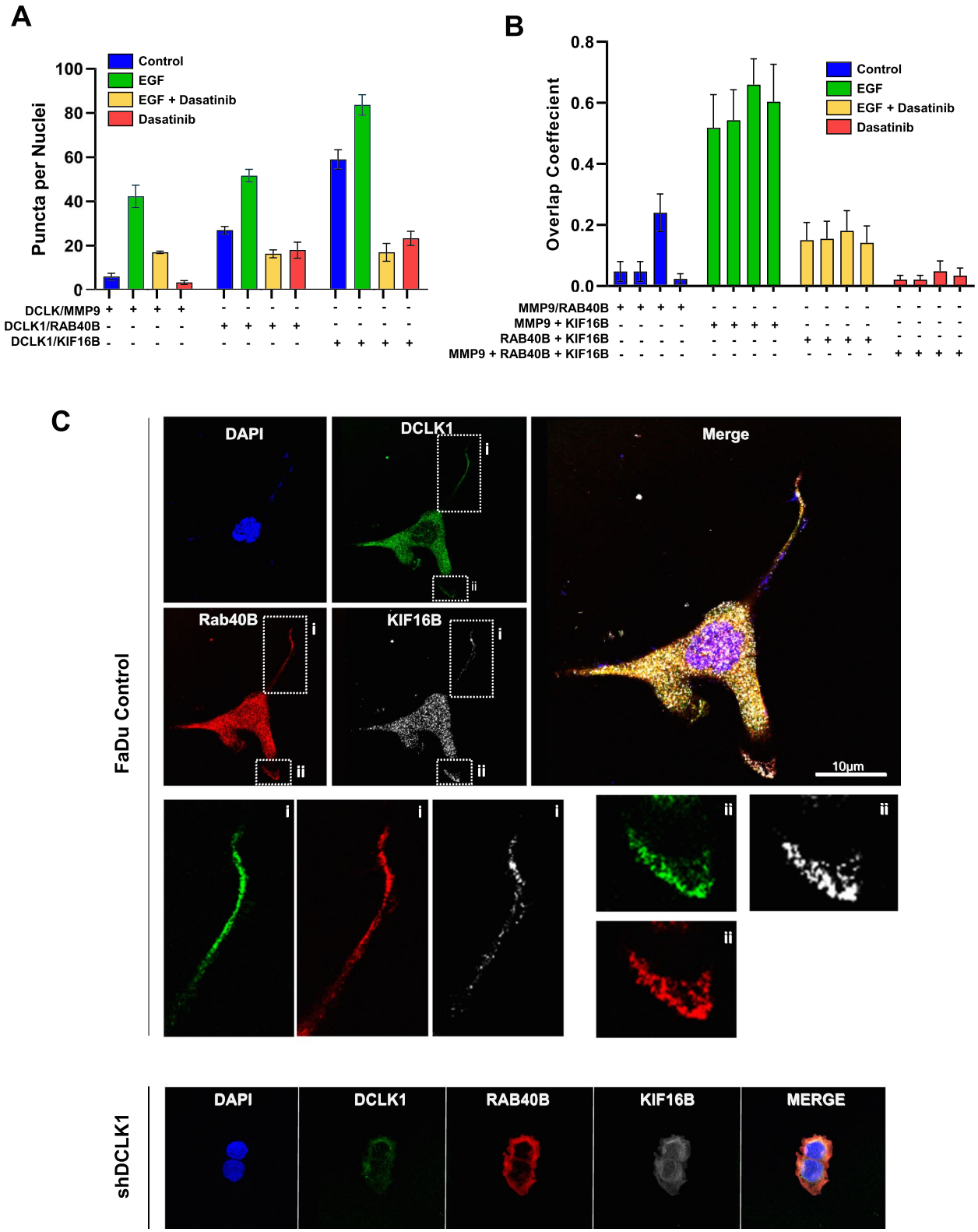

Fig. 6 (See legend on previous page.)

that DCLK1 knockdown leads to a reduction in EGFR protein and mRNA levels suggests that DCLK1 may play a critical role in regulating EGFR expression. DCLK1 overexpression has been reported to contribute to EGFR tyrosine kinase resistance in lung cancer cells through the regulation of Wnt-β-catenin signaling [67]. Future studies will need to explore the molecular regulators including Wnt-β-catenin that affect EGFR transcription and translation in DCLK1 regulated HNSCC.

Given that KIF16B is known to facilitate the early endosomal transport and recycling of cell surface receptors, including EGFR, it is plausible that DCLK1 knockdown disrupts the function of KIF16B. This disruption could impair the recycling of EGFR, leading to its accelerated degradation rather than its return to the cell surface, thereby resulting in decreased overall levels of EGFR. This hypothesis aligns with previous findings where inhibition of KIF16B function accelerated EGFR degradation by preventing its proper recycling [68]. Further investigations are needed to delineate the exact molecular interactions between DCLK1 and KIF16B in this context.

Furthermore, the interplay between DCLK1 and the Kinesin 3 superfamily, which encompasses KIF16B, is responsible for directing dense core vesicles towards the microtubule plus end [17].

While our study provides significant insights into the role of DCLK1 in invadopodia dynamics and MMP trafficking, there are limitations that need to be acknowledged. One is the absence of in vivo animal studies validating our findings in a more complex biological environment. The challenges associated with imaging sub-cellular structures in live mice are significant. Additionally, although we have discussed the dynamic nature of invadopodia, our current study relies on static imaging techniques, which do not capture the real-time formation and function of these structures. Another limitation is the absence of data on overexpression of DCLK1 in HNSCC cells. In our experience, even low levels of DCLK1 in HNSCC has a high impact on regulating the invasive ability of the cells. Hence, we focused on knocking down the endogenous levels to assess the impact on invasion. In future studies, we will examine the effects of DCLK1 overexpression in HNSCC.

In addition to regulating the trafficking of matrix-degrading proteases, our data indicate that DCLK1 also contributes to the formation of invadopodia. Knockdown of DCLK1 reduced the number of invadopodia in HNSCC spheroids. Further, inhibition of DCLK1 with DiFiD, reduced the degradation of gelatin, matrigel and VitroGel by invadopodia. Finally, knockdown of DCLK1 reduced the localization of markers for mature invadopodia, including TKS4, TKS5, MMP14 and cortactin in the periphery of the cells. This dual functionality of DCLK1 in trafficking of MMP cargo to the tip of the invadopodia and formation of mature invadopodia, reinforces its role as a central mediator of HNSCC invasion and underscores the importance of considering both aspects when developing strategies to disrupt invadopodia-driven tumor progression.

Moreover, this study is the first to demonstrate a functional role for the microtubule-binding protein DCLK1 within invadopodia in HNSCC, proposing that DCLK1 actively drives the transport of degradative MMP9 cargo. Finally, our findings reveal a previously uncharacterized connection among DCLK1, KIF16B, MMP9, and the RAB40B complex, thereby broadening the understanding of invasion mechanisms and identifying potential targets for therapeutic intervention.

Materials and methods

Cells and reagents

In this study, well-defined cell lines derived from HNSCC were utilized. The cell lines used were FaDu (ATCC), CAL33 (cat# ACC 447 DSMZ; Braunschweig, Germany), and UMSCC1 (obtained from Dr. Thomas E Carey at the University of Michigan). The authentication of established cell lines was performed periodically at Johns Hopkins utilizing the Promega GenePrint 10 kit, and the analysis was conducted utilizing GeneMapper v4.0. Each cell line was cultured in DMEM (Corning) supplemented with 10% heat-inactivated FBS (Sigma-Aldrich) not including antibiotics. Incubation of cells was carried out at 37 °C with 5% CO2. Tissue Microarray (#HN483) was acquired from US Biomax, Inc. The following antibodies were used: DCLK1 (abcam 31704), DCLK1 647 Alexa Flour (abcam EPR6085) TKS4 (abcam122342), MMP9 (abcam 73734), MMP2 (abcam 92536), MMP1 (abcam 52631), MMP13 (abcam 219620) from Abcam (Cambridge, UK); TKS5 (NBP1-90454), KIF16B (NBP1-14157), KIF1A (NBP1-80033), KIF1B (NB100-57493), KIF1C (NBP1-85978), KIF26B (NBP1-90443) from Novus Biologicals (Centennial, CO). β-tubulin from Sigma-Aldrich; pan-actin (H0000059-K) from Abnova (Taipei, Taiwan); anti-rabbit IgG Dylight 680 (#35568), anti-rabbit IgG Dylight 488 (#35553), and anti-mouse IgG Dylight 800 (#35521) from ThermoFisher (Waltham, MA). Texas Red-X Phalloidin (T7471) and DAPI 1306 were used for nuclear counterstaining (ThermoFisher). VitroGel® 3D High Concentration hydrogel (TWG001) from The Well Bioscience (North Brunswick, NJ) was employed. The N-Terminal pFLAG 3 vector (Addgene) was employed for cloning the DCLK1 DCX DNA by restriction digest, utilizing NotI and BamHI restriction enzymes. Following transfection, FaDu HNSCC cell line was isolated using G418 sulfate salt at a concentration of 400 µg/ml. In relation to the DCX Domain, the primers utilized

for DCLK1 NotI were as such: Forward Primer (FP): 5′-GATCGCGGCCGCGATGTCCTTCGGCAGA-3′, and Reverse Primer (RP): 5′-GATCGGATCCCTAGCCAT CGTTCTCATC-3′. For tandem mass tagged isobaric labeling, the TMT10plex (90110) kit from ThermoFisher was employed. DCLK1 was silenced using a well characterized specific siRNA targeting the coding region of DCLK1 (Thermo Fisher Scientific, cat # 4392420, assay ID: s17586), designed based on the reference sequence (accession No. NM_004734.4) [69]. A scrambled siRNA (Thermo Fisher Scientific, cat # AM4636) was used as a negative control.

Immunoblot

Cellular proteins were obtained by extracting whole-cell lysates using RIPA lysis buffer enhanced by addition of phosphatase and protease inhibitors (Roche 11,836,153,001). To remove debris, the cells were sonicated while on cold blocks and centrifuged, and the resulting supernatants were kept at −80 °C. Subsequently, the protein from cells were parted by electrophoresis on 10% SDS–polyacrylamide gels and moved onto PVDF membranes. To prevent nonspecific binding, the membranes were blocked using a mixture of TBS Intercept blocking buffer (Licor 927–60,050) and TBS in a 1:1 ratio. Primary antibodies, diluted in a 1:1 blocking buffer to TBST, were then incubated overnight with the membranes. Banding from protein was visualized using the LI-COR Odyssey DLx method and quantified utilizing ImageJ.

Mass spectrometry

FaDu cells (5×10^7 cells) with shControl or shDCLK1 were plated in 145-mm dishes with five dishes per condition for 24 h. Cells were trypsinized, washed thrice with 1X HBSS and centrifuged at 1200 rpm for 10 min at 4 °C. Cell pellets were shipped on ice to the IDEA National Center for Proteomics Core, University of Arkansas for Medical Sciences. Total protein from each cell pellet was reduced, alkylated, and purified by chloroform/methanol extraction prior to digestion with sequencing grade modified porcine trypsin (Promega). Tryptic peptides were labeled using a tandem mass tag 10-plex isobaric label reagent set (Thermo) and enriched using High-Select TiO2 and Fe-NTA phosphopeptide enrichment kits in succession (Thermo) following the manufacturer's instructions. Both enriched and un-enriched labeled peptides were separated into 46 fractions on a 100×1.0 mm Acquity BEH C18 column (Waters) using an UltiMate 3000 UHPLC system (Thermo) with a 40 min gradient from 99:1 to 60:40 buffer A:B ratio under basic pH conditions, and then consolidated into 18 super-fractions. Each super-fraction was then further separated by reverse phase XSelect CSH C18 2.5 um resin (Waters) on an in-line 150×0.075 mm column using an UltiMate 3000 RSLCnano system (Thermo). Peptides were eluted using a 60 min gradient from 98:2 to 60:40 buffer A:B ratio.Eluted peptides were ionized by electrospray (2.4 kV) followed by mass spectrometric analysis on an Orbitrap Eclipse Tribrid mass spectrometer (Thermo) using multi-notch MS3 parameters. MS data were acquired using the FTMS analyzer in top-speed profile mode at a resolution of 120,000 over a range of 375 to 1500 m/z. Following CID activation with normalized collision energy of 31.0, MS/MS data were acquired using the ion trap analyzer in centroid mode and normal mass range. Using synchronous precursor selection, up to 10 MS/MS precursors were selected for HCD activation with normalized collision energy of 55.0, followed by acquisition of MS3 reporter ion data using the FTMS analyzer in profile mode at a resolution of 50,000 over a range of 100–500 m/z.Buffer A = 0.1% formic acid, 0.5% acetonitrile;Buffer B = 0.1% formic acid, 99.9% acetonitrile.Both buffers adjusted to pH 10 with ammonium hydroxide for offline separation.

Mass spectrometry data analysis – ProteoViz (phosphoTMT)

Proteins were identified and reporter ions quantified by searching the UniprotKB database restricted to Homo sapiens (January 2022) using MaxQuant (Max Planck Institute, version 2.0.3.0) [70] with a parent ion tolerance of 3 ppm, a fragment ion tolerance of 0.5 Da, a reporter ion tolerance of 0.001 Da, trypsin/P enzyme with 2 missed cleavages, variable modifications including oxidation on M, Acetyl on Protein N-term, and phosphorylation on STY, and fixed modification of Carbamidomethyl on C. Protein identifications were accepted if they could be established with less than 1.0% false discovery. Proteins identified only by modified peptides were removed. Protein probabilities were assigned by the Protein Prophet algorithm [71]. TMT MS3 reporter ion intensity values are analyzed for changes in total protein using the unenriched lysate sample. Phospho (STY) modifications were identified using the samples enriched for phosphorylated peptides. The enriched and un-enriched samples are multiplexed using two TMT10-plex batches, one for the enriched and one for the un-enriched samples.

Following data acquisition and database search, the MS3 reporter ion intensities were normalized using ProteiNorm [72]. The data was normalized using VSN [73] and analyzed using proteoDA to perform statistical analysis using Linear Models for Microarray Data (limma) with empirical Bayes (eBayes) smoothing to the standard errors [74]. A similar approach is used for differential analysis of the phosphopeptides, with the addition

of a few steps. The phospho sites were filtered to retain only peptides with a localization probability > 75%, filter peptides with zero values, and log2 transformed. Limma was also used for differential analysis. Proteins and phosphopeptides with an FDR-adjusted p-value < 0.05 and an absolute fold change > 2 were considered significant.

Proteomic and phospho-proteomic integrative analysis

An established cutoff of log2-fold change greater than 1.0 with a p-value < 0.05 was used. To evaluate biological processes, gene ontology, and pathway networks associated with total protein data, the ShinyGO tool was employed [75]. Top-level enriched gene ontology terms and biological pathways were determined by inputting differential proteins into Metascape [19]. Kinase enrichment analysis was performed using KEA3 [24]. The CORAL tool was used to establish the kinome tree and quantitatively evaluate kinase interactions [25]. For determining kinase activity through functional networks, the RoKAI app was utilized, and the beta version of RoKAI Explorer was employed to determine the functional ontology related to phosphor-kinases [26].

Gelatin invadopodia assay

HNSCC cells were pretreated with either 10 nM DiFiD or vehicle control for 2 h prior to seeding. The QCM Gelatin Invadopodia Assay was performed and quantified following the manufacturer's instructions (Millipore, ECM670) and performed as previously reported [76]. Briefly, 20,000 pretreated cells were plated per well in an 8-well chamber slide (ibidi 80827) pre-coated with FITC-labeled matrices, where gelatin was labeled at a molar ratio of 1:50, Matrigel at 1:100, and VitroGel at 1:80. DCLK1 was visualized using Alexa Fluor 647 conjugation, and actin filaments were labeled with TRITC-phalloidin (1:1000) provided in the kit. Confocal images were captured at 100× objective magnification using oil immersion to analyze degradation spots and the colocalization of DCLK1 with actin at sites of gelatin degradation.

Invadopodium assay

An angiogenesis chamber slide (Ibidi, 81506) was prepared by diluting VitroGel® 3D High Concentration hydrogel (The Well Bioscience, TWG001) at a concentration of 10 mg/ml in a 1:2 ratio with DMEM + 10% FBS to achieve a final hydrogel concentration of 3 mg/ml at room temperature. This mixture was then incubated at 37 °C to polymerize in the innermost well. The VitroGel mixture achieves a stiffness of 600–1000 Pa, mimicking the extracellular matrix conditions more representative of the tumor microenvironment than the stiffness on a 2D surface. Cells suspended in 10 µL of VitroGel were seeded onto the polymerized hydrogel layer at 50% confluence. The setup was then incubated at 37 °C for 30 min to allow the gel to fully polymerize. Subsequently, an additional 30 µL of VitroGel was applied over the cells to encase the cells within the matrix and incubated again at 37 °C for 30 min. The matrix containing cells was fixed 12 h post-seeding with 4% paraformaldehyde (PFA) for staining, and then examined either by confocal imaging or observed under bright-field microscopy.

Boyden chamber invasion assay

Cell invasion was evaluated using the transwell Boyden chamber system, following our previously reported protocol [77]. In brief, a thin layer of VitroGel (50 µL) was applied to inserts with 8-µm pores. HNSCC cells (3×10^4 cells/well) in serum-free DMEM were plated on the VitroGel-coated inserts. These inserts were then set in triplicate containment wells containing media containing serum up to 24 h. Simultaneously, cells (2×10^3 cells/well in a 96-well plate) were plated under identical conditions to assess viability using the CyQUANT assay (Invitrogen C7026) pursuant to the manufacturer's guidelines. Cells were fixed and stained with the Hema 3 kit (Thermo Fisher Scientific), cells in the insert were removed with a cotton tipped applicator and the invading cells were counted. The number of invading cells was normalized based on cell viability.

Co-immunoprecipitation

Co-immunoprecipitation was performed using FaDu and UMSCC1 cells (5×10^7 cells in 145-mm dishes per treatment condition) to investigate the interaction between DCLK1, KIF16B, and RAB40B as previously described [78, 79]. After culturing the cells in serum-containing media for 24 h, they were serum-starved for an additional 24 h. Following serum starvation, the cells were treated with DiFiD (10 nM for 2 h), EGF (10 ng/mL for 5 min), a combination of DiFiD and EGF, or DMSO as a control. Cells were lysed using the detergent lysis method, and protein concentration was determined using the Bradford assay. For each immunoprecipitation, 500 µg of total protein was incubated with 5 µg of antibodies against DCLK1, KIF16B, or RAB40B. The antibodies were pre-coupled to Dynabeads® M-270 Epoxy using the Dynabeads® Co-Immunoprecipitation Kit (Thermo Fisher Scientific 14321D). The protein-antibody complexes were incubated overnight at 4 °C with gentle rotation to ensure optimal binding. Following incubation, the Dynabeads® were magnetically separated, and the supernatant was removed. The beads were washed three times with the provided washing buffer to remove non-specifically bound proteins. Bound proteins were then eluted from the beads using the elution buffer provided in the kit. Eluted proteins were subjected to SDS-PAGE

and analyzed by Western blotting to detect co-immunoprecipitated proteins. DiFiD treatment was used to assess its effect on the interaction between DCLK1 and KIF16B, with the same procedure applied to treated samples.

Gel zymography

Gel zymography analysis was performed using 10% Zymogram gels (Novex ZY00100BOX) according to the manufacturer's instructions and previously reported literature [80]. Briefly, HNSCC cells (3×10^5 cells/well in a 60-mm dish) were cultured in DMEM containing 10% FBS for 24 h, followed by a 24-h serum starvation period. After serum starvation, cells were treated with EGF (10 ng/mL for 5 min), dasatinib (100 nM for 2 h), a combination of EGF and dasatinib, DiFiD (10 nM for 2 h), a combination of EGF and DiFiD, or DMSO as a control. Following treatment, cells were washed with PBS and cultured for an additional 12 h in serum-free media before collecting the conditioned media. The conditioned media was concentrated (Pierce 88527), and protein concentration was determined using a Bradford colorimetric assay. Conditioned media containing 50 µg of protein from shDCLK1 or shControl FaDu cells was subjected to electrophoresis at a constant voltage of 125 V for 90 min. After electrophoresis, the gel was incubated at room temperature for one hour in renaturing buffer (Novex LC2670), followed by an overnight incubation in developing buffer (Novex LC2671). The gel was then stained using SimplyBlue Safestain (Thermo LC6060). Clear bands on the gel indicated areas of protease activity, while the background remained blue, signifying areas without protease activity.

Dye quenched assay

A volume of 10 µL of VitroGel (The Well Biosciences VHM01), saturated with 50 µg/ml of pigskin DQ-gelatin (Thermo D12054), was polymerized in the central well of an angiogenesis chamber slide (Ibidi 81506). Subsequently, gel coverslips were prepared by seeding 2×10^5 cells and incubating them at 37 °C to allow degradation for 12 h. Following incubation, the cells were fixed using 4% paraformaldehyde in PBS. Quantification of matrix degradation was performed by assessing the number of degraded spaces in 15 cellular fields (300–500 cells) for every experimental condition.

To quantify ECM degradation using DQ-gelatin, a plate reader method was utilized as previously described [81]. The assay was performed in a 96-well black, clear-bottom plate (Greiner Bio-One). A 40 µL volume of VitroGel, saturated with 50 µg/mL pigskin DQ-gelatin, was evenly spread in each well and allowed to polymerize for 20 min at 37 °C. UMSCC1 and CAL33 HNSCC cells (1×10^4), with and without DCLK1 knockdown, were seeded on top of the DQ-gelatin-impregnated VitroGel and incubated in serum-free DMEM for 12 h at 37 °C. Fluorescence was measured at 12, 18, and 24 h using a BioTek Synergy microplate reader (Agilent, model HTX) with excitation at 485 nm and emission at 530 nm. In a separate experiment, HNSCC cells were treated with 2 nM erlotinib, 10 ng/mL EGF, 10 nM DiFiD, DMSO control, or a combination of these treatments and seeded on the DQ-gelatin substrate for 12 h before fluorescence measurements were taken.

Enzyme-linked immunosorbent assay (ELISA)

To determine the levels of secreted MMP9, FaDu HNSCC cells (5×10^7 cells/well in a 145-mm dish), with or without DCLK1 knockout, were seeded in DMEM containing 10% FBS and cultured for 24 h. Afterward, the cultures were washed with PBS and incubated in serum-free DMEM for 12 h. To assess the effects of EGF stimulation and dasatinib inhibition, cells were treated with EGF (10 ng/mL for 5 min), dasatinib (100 nM for 2 h), a combination of dasatinib and EGF, or DMSO as a control. Following treatment, cells were cultured for an additional 12 h. Conditioned media was then collected, and protein concentrations were normalized using a Bradford assay. MMP9 levels were quantified using the Quantikine ELISA kit (DMP900, R & D Systems) according to the manufacturer's instructions. The assay signal was detected using a BioTek Synergy microplate reader (Agilent, model HTX).

To determine the levels of intracellular MMP9 levels in FaDu, UMSCC1, and CAL33 cells (2×10^5 cells/well in a T75 flask), with or without DCLK1 knockout, cells were seeded in DMEM containing 10% FBS and cultured for 24 h. Afterward, the cultures were washed with PBS and incubated in serum-free DMEM for 12 h without any additional treatment. Cells were then harvested, and cell lysates were generated by cell scraping, sonication, and centrifugation at $12{,}000\times g$ for 15 min at 4 °C. The lysate supernatant was normalized using a Bradford assay, and MMP9 levels were quantified using the MMP9 Quantikine ELISA kit (DMP900, R & D Systems) according to the manufacturer's instructions. The assay signal was detected using a BioTek Synergy microplate reader (Agilent, model HTX).

Proximity ligation assay

Cells were seeded in VitroGel at 50% confluence on 8 well chamber slides (ibidi 80826) for PLA (Proximity Ligation Assay) using the Duolink in situ Detection Reagents Red kit (DUO92008, Sigma-Aldrich), following the given protocol. Various groupings of primary antibodies targeting DCLK1 and KIF16B, KIF1A, KIF1B, KIF1C, KIF26B, MMP1, MMP9, or RAB40B were employed.

Subsequently, PLA puncta were imaged utilizing a TCS SP8 confocal laser scanning microscope (Leica Microsystems) equipped with a 40×1.35 NA or 100×1.35 NA oil immersion objective. High-resolution z-stack photograms were captured with a z-interval of 0.5 µm. Two-dimensional projections were generated using the LAX software platform (Leica Microsystems) by combining the maximum intensity from each z-series. The density of PLA puncta was determined by analyzing high-resolution images (captured with a 40×1.35 NA objective) using ImageJ (NIH).

Human MMP antibody array

The evaluation of human MMPs and tissue inhibitors of metalloproteinases (TIMPs) was conducted following the instructions provided by the manufacturer (Abcam 134004). In summary, 200 µg of total protein derived from CM of shDCLK1 or shControl FaDu cells was applied to separate blot arrays and incubated overnight. The arrays were subsequently subjected to chemiluminescence detection, and the resulting signals were captured at different exposure times.

The cancer genome atlas data analysis

The gene expression RNAseq data of the TCGA head and neck cancer (HNSC) Firehose Legacy cohort was obtained using cBioPortal [82, 83]. The expression levels of DCLK1 were categorized as elevated to suppressed based on their relationship to the median quantification of gene-level transcripts estimated, which were converted using log2(x+1) and normalized using RSEM counts. These expression levels were then matched with clinical lymph node staging data obtained from TCGA.

Immunofluorescence colocalization analysis

Quantitative analysis of protein colocalization was performed on the confocal microscopy images as previously described [43]. Briefly, all image processing steps were performed with the FIJI distribution of ImageJ (version 1.54j). Each image was preprocessed with sequential denoising, despeckling, and 8-bit conversion. Histogram equalization was then performed via the Contrast Limited AHE (CLAHE) method. Background subtraction was achieved with a rolling ball algorithm. Regions of interest (ROIs) containing cell clusters were generated via segmentation of merged images for each condition. For the banded segmentation analysis, an adaptation of the protocol described previously described by Pike et al., Methods 2017 [43]. Initial cellular ROI was eroded in 1um intervals based on the Euclidean distance from the segmentation edge. Volume contained with the boundaries of each band were isolated and evaluated for colocalization of fluorescent signal. Thresholds were automatically generated via the Costes' algorithm and Pearson's R and Manders' coefficients were extrapolated in Python (version 3.12.0).

In silicomodeling

Complexes of the kinase domain of DCLK1 (residues 390–647) with the motor domain (3–358) and peptide segments from KIF16B (652–672 and 1016–1035) along with the SOCS box (175–228) and two other constructs (175–260 and 230–278) of RAB40B were modeled using Alphafold3 [84]. In each case, one ATP molecule and two Mg+2 ions were specified. Confidence metrics and visual inspection for a serine or threonine near the active were used to select a model from each ensemble of predictions with a high confidence prediction.

Statistical analysis

The data are presented as the mean ± standard error of the mean (SEM). Significance in all experiments was assessed using non-parametric two-tailed Mann–Whitney U tests, and for comparison of multiple groups, the Kruskal–Wallis test was used. All statistical calculations were conducted via GraphPad Prism Software (version 9.1.0), and significance was decided by a p-value less than 0.05.

Supplementary Information

The online version contains supplementary material available at https://doi.org/10.1186/s12943-025-02264-3.

Supplementary Material 1.

Supplementary Material 2.

Supplementary Material 3.

Supplementary Material 4.

Supplementary Material 5: Figure 1. Protein expression in DCLK1 knockdown cells is distinct. Principal component analysis (PCA) was conducted on mass spectrometry data to visualize distinct clusters and dendrogram representation of both (A) total protein and (B) phosphopeptide populations. The plot exhibits clear separation between shControl (n=5) and shDCLK1 (n=5) samples, indicating distinct population patterns based on the analyzed data.

Supplementary Material 6: Figure 2. DCLK1 drives cell movement and cytoskeletal dynamics. Protein clusters displaying alterations between shControl and shDCLK1 cells were subjected to enriched ontology analysis using Metascape [19]. (A) The bar graph illustrates the top 20 clusters of Gene Ontology top-level enriched terms in biological processes, with each cluster color-coded based on its respective p-value. (B) A depiction of top-level Gene Ontology biological processes provides a comprehensive overview of the enriched terms. The analysis and images were generated using Metascape [19]. (C) Gene ontology analysis using DAVID on differential expression of the 100 most significant phosphoproteins relative to the total protein in the control group relative to the DCLK1 knockdown group. Standard stringency settings were used to identify gene ontology terms related to cellular structure and function.

Supplementary Material 7: Figure 3. DCLK1 is associated with kinases involved in cell movement and invasion. (A) MeanRank results from KEA3 were visualized in a bar chart, emphasizing proteins enriched in shControl cells compared to shDCLK1 knockout cells. The chart presents the top

ten kinases, with bars color-coded to denote the selected libraries. The integrated ranking of predicted kinases is based on MeanRank scores, and the analysis, as well as the image, was generated using KEA3 [24]. (B) A phylogenetic kinase tree is presented to compare kinase activities between the shControl and shDCLK1 groups. The tree generated using the Coral kinome tool, features nodes representing different kinases. Node color signifies protein abundance, with blue indicating increased relative abundance in the shControl group and red indicating increased relative abundance in the shDCLK1 group. The node size reflects the log2 fold change. Branches of the tree are color-coded to highlight kinase groups showing associations between the two groups. The kinome analysis and kinase tree were generated using the CORAL web app [25].

Supplementary Material 8: Figure 4. DCLK1 knockdown is associated with reduced EGFR expression. (A) Western blot analysis showing protein expression levels of DCLK1 and EGFR in UMSCC1, CAL33, and FaDu cell lines. β-Tubulin was used as a loading control to ensure equal protein loading. (B) mRNA levels of DCLK1 and EGFR in cells treated with DCLK1 knockdown via shRNA (orange) or shRNA (blue), shown as fold change relative to their respective controls (dotted line at 1.0). Expression levels were measured and normalized to control levels. Data represent mean ± standard error (SE), with statistical significance indicated: (*$p < 0.05$, **$p < 0.01$). (C) TCGA analysis of HNSCC patients demonstrating the correlation between EGFR and DCLK1 expression with advancing tumor stage. The Pearson correlation coefficients for stages 1 through 4 were as follows: stage 1 ($r = 0.12$, $p = 0.725$), stage 2 ($r = 0.06$, $p = 0.776$), stage 3 ($r = 0.22$, $p = 0.251$), and stage 4 ($r = 0.29$, $p < 0.0001$).

Supplementary Material 9: Figure 5: DCLK1 Expression Increases Toward the Invasive Front in HNSCC Tissues and Is Consistently Expressed Across HNSCC Cell Lines. (A) Immunohistochemical (IHC) analysis showing DCLK1 expression in HNSCC tissue. The intensity of DCLK1 staining increases from the tumor core toward the invasive front. The line graph quantifies the cumulative staining intensity along the red lines drawn on the tissue section (left panel), with the trend line demonstrating the increase in expression toward the invasive front. (B) Representative IHC image showing minimal DCLK1 expression in adjacent normal mucosal tissue. (C) IHC image highlighting high DCLK1 expression in collective invasive strands (blue arrow), detached groups (red arrow), and individual cells (black arrow). (D) Schematic representation illustrating the assessment of invadopodia-mediated gelatin degradation in HNSCC cells. Top (XY) View depicts a cell on a gelatin-coated surface with highlighted areas of degradation. Orthogonal (XZ) View provides a side view schematic of the cell engaging in ECM degradation. Orthogonal Sectioning includes detailed schematic representations showing the colocalization of DCLK1 (cyan) and actin (magenta) within invadopodia at the sites of gelatin degradation (grayscale). Insets highlight orthogonal sections along the xz plane, offering a visual interpretation of the spatial distribution and activity of invadopodia components. Confocal images of UMSCC1 (E) and CAL33 (F) cells, captured using a 100x oil immersion objective. Images show DCLK1 (cyan) and actin (magenta) localization within invadopodia at sites of FITC-labeled gelatin degradation (grayscale), under control and DiFiD-treated conditions. Insets provide orthogonal (xz and yz) views, illustrating the structural details and spatial relationships of invadopodia components. (G) Schematic representation of the 3D invasion assay, illustrating the procedural steps to simulate the ECM environment for assessing invadopodia in HNSCC cells. The process involves preparing the lower well with ECM, followed by seeding cells in a suspension of ECM. After adding a top layer of ECM, the setup is incubated, and slides are prepared for imaging to analyze invadopodia function and ECM interaction. Gelatin (H), Matrigel (I), and VitroGel (J) are compared through confocal imaging of HNSCC cells to evaluate invadopodia dynamics. Each panel shows DCLK1 (cyan) and actin (magenta) localization, with insets providing orthogonal xz and yz views and strip charts illustrating consistent colocalization patterns across all matrices, indicating no significant differences in invadopodia behavior.

Supplementary Material 10: Figure 6: DCLK1 Colocalizes with Invadopodia Markers and Is Associated with Increased Gene Expression in HNSCC. (A) Line graph quantifying immunofluorescence images in Fig 3 G-J, showing distance-dependent colocalization analysis of DCLK1 with individual invadopodia markers: TKS4, TKS5, cortactin (CTTN), and MMP14. The analysis measures Manders scores M1 (DCLK1, green line) relative to the M2 (invadopodia marker, red line), and Pearson's correlation coefficient (R, blue line) across varying edge distances from 1.0 to 3.0 µm. (B) Bar graph of colocalization metrics across all invadopodia markers combined in Sup. Fig. 6A, analyzed at signal to cell edge distances of 1.0, 2.0, and 3.0 µm. The bars represent the average M1, M2, and Pearson's correlation coefficient. Immunofluorescence images of (C) FaDu, and (D) UMSCC1 cells showing colocalization of DCLK1 with invadopodia markers TKS4, TKS5, MMP14, and cortactin. (E) Comparative analysis of the colocalization metrics between DCLK1 and various invadopodia markers following DCLK1 knockdown (KD) versus control (CON) conditions in IF images from Sup. Fig 6C and D. The metrics analyzed include M1 (top left panel), M2 (top right panel), and Pearson's correlation coefficient (bottom panel). The invadopodia markers analyzed are TKS4, TKS5, MMP14, and cortactin (CTTN). The M1 metric (DCLK1) and M2 metric (invadopodia marker) display the relative colocalization intensities under KD versus CON conditions. Pearson's correlation coefficient quantifies the strength of the linear relationship between DCLK1 and each invadopodia marker. Confocal images display DCLK1 (cyan) colocalization with invadopodia markers in HNSCC cells over sites of gelatin degradation (grayscale), including TKS4 (F), TKS5 (G), MMP14 (H), and Cortactin (I), all highlighted in magenta. Red arrowheads point to areas where DCLK1 colocalizes with these markers directly over the degradation sites. (J) Box plots showing the levels of CTTN, SH3PXD2B, SH3PXD2A, and MMP14 genes (upper row) and proteins (lower row) in HNSCC compared to normal tissues, as derived from TCGA and CPTAC datasets, respectively. (K) Immunofluorescence images of proximity ligation assay results showing colocalization of DCLK1 with the invadopodia marker TKS4 in FaDu, UMSCC1, and CAL33 HNSCC cell lines. The images demonstrate that DCLK1 colocalizes with TKS4 within invadopodia structures across all three cell lines.

Supplementary Material 11: Figure 7: DCLK1 Colocalizes with Gelatin Degradation Sites and Promotes Gelatinase Activity in HNSCC Cell Lines. Immunofluorescence images showing colocalization of DCLK1 with gelatin degradation sites in FaDu (A), UMSCC1 (B), and CAL33 (C) cell lines. Cells were seeded on DQ-gelatin, which fluoresces upon degradation by gelatinases. DCLK1 was detected using a 647-conjugated antibody (red), and gelatin degradation was visualized using DQ-gelatin (green). The merged images show colocalization of DCLK1 with areas of gelatin degradation, indicated by white arrowheads in the zoomed-in sections, suggesting DCLK1's role in promoting gelatinase activity. (D) Confocal images comparing control and DCLK1 knockdown conditions in FaDu, UMSCC1, and CAL33 cell lines for DCLK1 (red), actin (gray), and DQ-gelatin (green). In control cells, DCLK1 colocalizes with actin and areas of gelatin degradation, whereas knockdown of DCLK1 significantly reduces both DCLK1 expression and the extent of gelatin degradation. Confocal imaging performed at 100X oil immersion objective. (E) Quantification of DQ-gelatin fluorescence intensity over time (12, 18, and 24 h) in UMSCC1 and CAL33 cell lines under control and DCLK1 knockdown conditions performed in a 96-well plate. The graph shows a significant reduction in gelatinase activity following DCLK1 knockdown, indicating that DCLK1 is crucial for maintaining gelatinase function in these cells. (F) Quantification of DQ fluorescence intensity in FaDu cells following treatment with EGF (10 ng/mL), the EGFR inhibitor erlotinib (2 nM), the DCLK1 inhibitor DiFiD (10 nM), or a combination of both erlotinib and DiFiD for 12 h (*$p < 0.05$, ****$p < 0.0001$).

Supplementary Material 12: Figure 8: DCLK1 Knockdown Reduces MMP Activity and Shows no Significant Interaction with MMP2 in HNSCC Cell Lines. (A) Gel zymography analysis of MMP activity in control and DCLK1 knockdown conditions in UMSCC1 and CAL33 cells treated with EGF (10 ng/mL for 5 min), Dasatinib (100 nM for 2 hours), combination EGF/Dasatinib, or DMSO control. (B) Gel zymography analysis in UMSCC1 and CAL33 cells, demonstrating pro-MMP-9 and active MMP-9 levels control and DCLK1 knockdown cells. (C) Gel zymography showing the effect of DiFiD (10 nM for 2 hours) treatment on MMP activity in UMSCC1 and CAL33 cells. (D) ELISA quantification of MMP-9 levels in cell lysates from UMSCC1, CAL33 cells treated with control or siDCLK1 and FaDu cells expressing control or shDCLK1. (E) Scatter plot from TCGA analysis showing the correlation between DCLK1 and MMP9 mRNA expression in HNSCC samples. The analysis reveals a weak positive correlation (Pearson correlation

coefficient = 0.16, *p*-value < 0.001). Immunofluorescence images of FaDu (F) and UMSCC1 (G) cells showing nuclei (DAPI, blue), DCLK1 (green) and MMP2 (red). Images captured utilizing 60x oil immersion objective.

Supplementary Material 13: Figure 9: DCLK1 Shows Minimal Colocalization with KIF1A, KIF1B, KIF1C, and KIF26B in HNSCC Cells. Immunofluorescence images of PLA data obtained using a 40x oil immersion objective demonstrate the colocalization analysis between DCLK1 and KIF1A, KIF1B, KIF1C, or KIF26B in HNSCC cells. The left column shows DAPI staining (blue) for nuclei, the middle column displays PLA signals (red), and the right column shows the merged images. Minimal colocalization was observed between DCLK1 and KIF1A, KIF1B, KIF1C, or KIF26B, indicating a lack of significant interaction between DCLK1 and these kinesins in HNSCC cells.

Supplementary Material 14: Figure 10: DCLK1 Forms Complexes with KIF16B and RAB40B, as Demonstrated by Proximity Ligation Assay and Co-Immunoprecipitation. (A) PLA data demonstrating the interaction between DCLK1 and KIF16B in HNSCC cells. The images show DAPI staining for nuclei (blue), PLA signals indicating DCLK1-KIF16B interactions (red), and the merged image with brightfield microscopy to visualize cell boundaries. Images captured with 100x oil immersion objective. (B) Co-immunoprecipitation (Co-IP) analysis of DCLK1 and KIF16B in FaDu and UMSCC1 cell lines treated with vehicle control, EGF (10 ng/mL for 5 min) and/or DiFiD (10 nM pretreated for 2 h). Input demonstrates total proteins in the cell lysates. Immunoblots (IB) were probed for KIF16B, RAB40B, and DCLK1.

Supplementary Material 15: Figure 11: EGF-Induced Colocalization of DCLK1 with KIF16B and TKS4 Is Disrupted by Dasatinib Treatment in HNSCC Cells. Immunofluorescence images showing the colocalization of DCLK1 (red), KIF16B (yellow), and TKS4 (green) in FaDu and UMSCC1 cells treated with EGF (10 ng/mL for 5 min), Dasatinib (100 nM for 2 hours), combination EGF/Dasatinib, or DMSO control. Images captured with 60x and 100x oil immersion objectives, respectively.

Supplementary Material 16: Figure 12. DCLK1, MMP9, RAB40B, and KIF16B form a complex. Multi-plex PLA in (A) FaDu, (B) UMSCC1, and (C) CAL33 to visualize the interactions between DCLK1 and MMP9, RAB40B, or KIF16B. Nuclear staining was performed using DAPI (blue), and positive interactions between DCLK1 and MMP9 are in yellow, between DCLK1 and RAB40B are in green and between DCLK1 and KIF16B are in red. Images were captured with oil immersion at a 40x objective.

Supplementary Material 17: Figure 13: Colocalization of DCLK1, RAB40B, and KIF16B in HNSCC Cells. Immunofluorescence images showing the colocalization of DCLK1, RAB40B, and KIF16B in UMSCC1 cells. The top row displays the following channels: DAPI (blue) for nuclei, DCLK1 (green), RAB40B (red), KIF16B (grey), and the merged image showing the colocalization of all three proteins. The bottom row provides zoomed-in views of a single cell invadopodia, highlighting the overlapping regions where DCLK1, RAB40B, and KIF16B colocalize. Images captured at 100x oil immersion objective.

Supplementary Material 18: Figure 14. Alphafold3 models of DCLK1 with KIF16 and RAB40B. Models of DCLK (green) with residues (A) 652-672 or (B) 1016-1035 of KIF16 (cyan). Polar contacts are shown as yellow dashes, and the backbone and/or side chain residues are shown as sticks. Interacting residues are labeled, with KIF16 residues italicized. The serine or threonine that could be phosphorylated is shown in spheres. ATP is shown in magenta sticks, while Mg+2 ions are green spheres. Alphafold3 model of DCLK1 with RAB40B (C) Models of DCLK (green) with residues 230-249 of RAB40B (cyan). Polar contacts are shown as yellow dashes, and the backbone and/or side chain residues are shown as sticks. Interacting residues are labeled, with RAB40B residues italicized. The serine or that could be phosphorylated is shown in spheres. ATP is shown in magenta sticks, while Mg+2 ions are green spheres.

Supplementary Material 19.

Acknowledgements
Biomedical Research Training Program at the University of Kansas Medical Center supported graduate researcher stipend expenses during the formation of this work.

Authors' contributions
L.A. conceived the work, designed experiments, performed experiments, and wrote the draft manuscript; M.Y., N.F., L.J., M.B., T.L., A.M., J.P.G., P.A, C.T., A. P., A.K.W., designed and performed experiments; M.P.W. designed and oversaw proteomic experiments and analysis; D.S., L.L., S.U. contributed to the design of the work; D.J. oversaw and executed Alphfold3 modeling; N.K.Y. contributed to data set analysis including TCGA analysis, representation, and statistical analysis; S.A. designed and participated in the conception of the work, assisted in manuscript preparation, and shared resources. S.M.T. designed and conceived the work, assisted manuscript preparation, supervised and facilitated all aspects of the work within.

Funding
This study was supported in part by the University of Kansas Cancer Center under CCSG P30CA168524; IDeA National Resource for Quantitative Proteomics and NIH/NIGMS grant LR24GM137786; The Leica STED microscope is supported by NIH S10OD023625 at the University of Kansas Medical Center, Kansas City, KS 66160. Biomedical Research Training Program at the University of Kansas Medical Center supported graduate researcher (LA) stipend expenses during the formation of this work.

Data availability
Data is provided within the manuscript or supplementary information files.

Declarations

Consent for publication
All authors give their consent for publication of this study.

Competing interests
The authors declare no competing interests.

Author details
[1]Department of Otolaryngology, Rainbow Blvd, University of Kansas Medical Center, 3901aq, Wahl Hall East 4031, Kansas, KS 66160, USA. [2]Department of Cancer Biology, Medical Center, University of Kansas, Kansas, KS 66160, USA. [3]Department of Biostatistics and Data Science, Medical Center, University of Kansas, Kansas, KS 66160, USA. [4]Computational Chemical Biology, University of Kansas, Lawrence, KS 66047, USA. [5]Stowers Institute, Kansas, MO, USA. [6]Department of Surgery, Medical Center, University of Kansas, Kansas, KS 66160, USA.

Received: 12 April 2024 Accepted: 6 February 2025
Published online: 24 February 2025

References

1. Ruff CA, et al. Neuronal c-Jun is required for successful axonal regeneration, but the effects of phosphorylation of its N-terminus are moderate. J Neurochem. 2012;121(4):607–18.
2. Yu SS, Cirillo N. The molecular markers of cancer stem cells in head and neck tumors. J Cell Physiol. 2020;235(1):65–73.
3. Najafi M, Farhood B, Mortezaee K. Extracellular matrix (ECM) stiffness and degradation as cancer drivers. J Cell Biochem. 2019;120(3):2782–90.
4. Marchisio P, et al. Cell-substratum interaction of cultured avian osteoclasts is mediated by specific adhesion structures. J Cell Biol. 1984;99(5):1696–705.
5. Monsky WL, et al. Binding and localization of M r 72,000 matrix metalloproteinase at cell surface invadopodia. Can Res. 1993;53(13):3159–64.
6. Linder S, Cervero P, Eddy R, Condeelis J. Mechanisms and roles of podosomes and invadopodia. Nat Rev Mol Cell Biol. 2023;24(2):86–106.
7. Oser M, Condeelis J. The cofilin activity cycle in lamellipodia and invadopodia. J Cell Biochem. 2009;108(6):1252–62.
8. Branch KM, Hoshino D, Weaver AM. Adhesion rings surround invadopodia and promote maturation. Biology open. 2012;1(8):711–22.
9. Masi I, Caprara V, Bagnato A, Rosanò L. Tumor cellular and microenvironmental cues controlling invadopodia formation. Frontiers in Cell and Developmental Biology. 2020;8: 584181.

10. Revach O-Y, et al. Mechanical interplay between invadopodia and the nucleus in cultured cancer cells. Sci Rep. 2015;5(1):9466.
11. Buschman MD, et al. The novel adaptor protein Tks4 (SH3PXD2B) is required for functional podosome formation. Mol Biol Cell. 2009;20(5):1302–11.
12. Sharma VP, et al. Tks5 and SHIP2 regulate invadopodium maturation, but not initiation, in breast carcinoma cells. Curr Biol. 2013;23(21):2079–89.
13. Jacob A, et al. The role and regulation of Rab40b–Tks5 complex during invadopodia formation and cancer cell invasion. J Cell Sci. 2016;129(23):4341–53.
14. May R, et al. Identification of a novel putative gastrointestinal stem cell and adenoma stem cell marker, doublecortin and CaM kinase-like-1, following radiation injury and in adenomatous polyposis coli/multiple intestinal neoplasia mice. Stem cells. 2008;26(3):630–7.
15. Standing D, et al. Doublecortin-like kinase 1 is a therapeutic target in squamous cell carcinoma. Mol Carcinog. 2023;62(2):145–59.
16. Burgess HA, Reiner O. Doublecortin-like Kinase Is Associated with Microtubules in Neuronal Growth Cones. Mol Cell Neurosci. 2000;16(5):529–41.
17. Lipka J, Kapitein LC, Jaworski J, Hoogenraad CC. Microtubule-binding protein doublecortin-like kinase 1 (DCLK1) guides kinesin-3-mediated cargo transport to dendrites. Embo j. 2016;35(3):302–18.
18. Körner S, et al. Antagonizing Sec62 function in intracellular Ca(2+) homeostasis represents a novel therapeutic strategy for head and neck cancer. Front Physiol. 2022;13: 880004.
19. Zhou Y, et al. Metascape provides a biologist-oriented resource for the analysis of systems-level datasets. Nat Commun. 2019;10(1):1523.
20. Sherman BT, et al. DAVID: a web server for functional enrichment analysis and functional annotation of gene lists (2021 update). Nucleic Acids Res. 2022;50(W1):W216-w221.
21. Stark, C., et al., BioGRID: a general repository for interaction datasets. Nucleic Acids Res, 2006. 34(Database issue):D535–9.
22. Chatr-aryamontri, A., et al., MINT: the Molecular INTeraction database. Nucleic Acids Res, 2007. 35(Database issue):D572–4.
23. Szklarczyk D, et al. The STRING database in 2023: protein-protein association networks and functional enrichment analyses for any sequenced genome of interest. Nucleic Acids Res. 2023;51(D1):D638-d646.
24. Kuleshov MV, et al. KEA3: improved kinase enrichment analysis via data integration. Nucleic Acids Res. 2021;49(W1):W304–16.
25. Metz KS, et al. Coral: Clear and Customizable Visualization of Human Kinome Data. Cell Syst. 2018;7(3):347-350.e1.
26. Yılmaz S, et al. Robust inference of kinase activity using functional networks. Nat Commun. 2021;12(1):1177.
27. Chen WT. Proteolytic activity of specialized surface protrusions formed at rosette contact sites of transformed cells. J Exp Zool. 1989;251(2):167–85.
28. Augoff K, Hryniewicz-Jankowska A, Tabola R. Invadopodia: clearing the way for cancer cell invasion. Ann Transl Med. 2020;8(14):902.
29. Burger KL, et al. The podosome marker protein Tks5 regulates macrophage invasive behavior. Cytoskeleton. 2011;68(12):694–711.
30. Díaz, B., Invadopodia Detection and Gelatin Degradation Assay. Bio Protoc, 2013. 3(24).
31. Shao Y, et al. PDZK1 protects against mechanical overload-induced chondrocyte senescence and osteoarthritis by targeting mitochondrial function. Bone Research. 2024;12(1):41.
32. Schor SL, et al. A novel "sandwich" assay for quantifying chemo-regulated cell migration within 3-dimensional matrices: wound healing cytokines exhibit distinct motogenic activities compared to the transmembrane assay. Cell Motil Cytoskeleton. 2006;63(5):287–300.
33. Haruna, N. and J. Huang, Investigating the dynamic Biophysical Properties of a tunable hydrogel for 3D cell culture. J. Cytol. Tissue Biol, 2020. 7(030):10.24966.
34. Zeiringer S, et al. Development and Characterization of an In Vitro Intestinal Model Including Extracellular Matrix and Macrovascular Endothelium. Mol Pharm. 2023;20(10):5173–84.
35. Baik J, et al. Induction of glioblastoma invasion triggered by system Xc−-mediated glutamate release. Mol Cell Toxicol. 2024;20(4):1025–34.
36. Shi L, et al. miR-34b-5p suppresses the epithelial-mesenchymal transition and metastasis in endometrial cancer AN3CA cells by targeting ZEB1. Int J Clin Exp Pathol. 2024;17(4):137–50.
37. Ishikawa-Ankerhold, H., et al., Centrosome Positioning in Migrating Dictyostelium Cells. Cells, 2022. 11(11).
38. Bowden ET, et al. An invasion-related complex of cortactin, paxillin and PKCμ associates with invadopodia at sites of extracellular matrix degradation. Oncogene. 1999;18(31):4440–9.
39. Jeannot P, Besson A. Cortactin function in invadopodia. Small GTPases. 2020;11(4):256–70.
40. Burger KL, et al. Src-dependent Tks5 phosphorylation regulates invadopodia-associated invasion in prostate cancer cells. Prostate. 2014;74(2):134–48.
41. Ferrari R, et al. MT1-MMP directs force-producing proteolytic contacts that drive tumor cell invasion. Nat Commun. 2019;10(1):4886.
42. Iizuka S, et al. The role of Tks adaptor proteins in invadopodia formation, growth and metastasis of melanoma. Oncotarget. 2016;7(48):78473–86.
43. Pike JA, Styles IB, Rappoport JZ, Heath JK. Quantifying receptor trafficking and colocalization with confocal microscopy. Methods. 2017;115:42–54.
44. Marwaha, R. and M. Sharma, DQ-Red BSA Trafficking Assay in Cultured Cells to Assess Cargo Delivery to Lysosomes. Bio Protoc, 2017. 7(19).
45. Makowiecka A, Simiczyjew A, Nowak D, Mazur AJ. Varying effects of EGF, HGF and TGFβ on formation of invadopodia and invasiveness of melanoma cell lines of different origin. Eur J Histochem. 2016;60(4):2728.
46. Thomas SM, et al. Epidermal growth factor receptor-stimulated activation of phospholipase Cgamma-1 promotes invasion of head and neck squamous cell carcinoma. Cancer Res. 2003;63(17):5629–35.
47. Nozawa H, et al. Combined inhibition of PLCgamma-1 and c-Src abrogates epidermal growth factor receptor-mediated head and neck squamous cell carcinoma invasion. Clin Cancer Res. 2008;14(13):4336–44.
48. Araujo J, Logothetis C. Dasatinib: a potent SRC inhibitor in clinical development for the treatment of solid tumors. Cancer Treat Rev. 2010;36(6):492–500.
49. Vermeer PD, et al. MMP9 modulates tight junction integrity and cell viability in human airway epithelia. Am J Physiol Lung Cell Mol Physiol. 2009;296(5):L751–62.
50. Abécassis I, et al. RhoA induces MMP-9 expression at CD44 lamellipodial focal complexes and promotes HMEC-1 cell invasion. Exp Cell Res. 2003;291(2):363–76.
51. Han J, et al. Additive effects of EGF and IL-1β regulate tumor cell migration and invasion in gastric adenocarcinoma via activation of ERK1/2. Int J Oncol. 2014;45(1):291–301.
52. Jacob A, Prekeris R. The regulation of MMP targeting to invadopodia during cancer metastasis. Front Cell Dev Biol. 2015;3:4.
53. Bartha, Á. and B. Győrffy, TNMplot.com: A Web Tool for the Comparison of Gene Expression in Normal, Tumor and Metastatic Tissues. Int J Mol Sci, 2021. 22(5).
54. Hornbeck PV, et al. PhosphoSitePlus, 2014: mutations, PTMs and recalibrations. Nucleic Acids Res. 2015;43(D1):D512–20.
55. Rosenthal EL, Matrisian LM. Matrix metalloproteases in head and neck cancer. Head Neck. 2006;28(7):639–48.
56. Iizuka, S., et al., Crosstalk between invadopodia and the extracellular matrix. bioRxiv, 2020: p. 2020.02.26.966762.
57. Chandrakesan, P., et al., Regulatory roles of Dclk1 in epithelial mesenchymal transition and cancer stem cells. J Carcinogenesis Mutagenesis, 2016. 7(2).
58. Kumar S, Das A, Barai A, Sen S. MMP Secretion Rate and Inter-invadopodia Spacing Collectively Govern Cancer Invasiveness. Biophys J. 2018;114(3):650–62.
59. Allen JL, et al. Evaluation of the matrix metalloproteinase 9 (MMP9) inhibitor Andecaliximab as an Anti-invasive therapeutic in Head and neck squamous cell carcinoma. Oral Oncol. 2022;132: 106008.
60. Quintero-Fabián, S., et al., Role of Matrix Metalloproteinases in Angiogenesis and Cancer. Frontiers in Oncology, 2019. 9.
61. Gonzalez-Avila G, Sommer B, García-Hernández AA, Ramos C. Matrix Metalloproteinases' Role in Tumor Microenvironment. In: Birbrair A, editor. Tumor Microenvironment: Extracellular Matrix Components – Part A. Cham: Springer International Publishing; 2020. p. 97–131.
62. Soppina V, et al. Dimerization of mammalian kinesin-3 motors results in superprocessive motion. Proc Natl Acad Sci. 2014;111(15):5562–7.
63. Hey S, Wiesner C, Barcelona B, Linder S. KIF16B drives MT1-MMP recycling in macrophages and promotes co-invasion of cancer cells. Life Science Alliance. 2023;6(11): e202302158.
64. Kumar D, et al. Mitigation of Tumor-Associated Fibroblast-Facilitated Head and Neck Cancer Progression With Anti-Hepatocyte Growth

Factor Antibody Ficlatuzumab. JAMA Otolaryngol Head Neck Surg. 2015;141(12):1133–9.
65. Yan X, et al. MT4-MMP promotes invadopodia formation and cell motility in FaDu head and neck cancer cells. Biochem Biophys Res Commun. 2020;522(4):1009–14.
66. Hwang YS, Park K-K, Chung W-Y. Invadopodia formation in oral squamous cell carcinoma: The role of epidermal growth factor receptor signalling. Arch Oral Biol. 2012;57(4):335–43.
67. Yan R, et al. Inhibition of DCLK1 sensitizes resistant lung adenocarcinomas to EGFR-TKI through suppression of Wnt/beta-Catenin activity and cancer stemness. Cancer Lett. 2022;531:83–97.
68. Hoepfner S, et al. Modulation of receptor recycling and degradation by the endosomal kinesin KIF16B. Cell. 2005;121(3):437–50.
69. Wang, J., et al., Functional assessment of miR-1291 in colon cancer cells. Int J Oncol, 2022. 60(2).
70. Tyanova S, Temu T, Cox J. The MaxQuant computational platform for mass spectrometry-based shotgun proteomics. Nat Protoc. 2016;11(12):2301–19.
71. Nesvizhskii AI, Keller A, Kolker E, Aebersold R. A statistical model for identifying proteins by tandem mass spectrometry. Anal Chem. 2003;75(17):4646–58.
72. Graw S, et al. proteiNorm - A User-Friendly Tool for Normalization and Analysis of TMT and Label-Free Protein Quantification. ACS Omega. 2020;5(40):25625–33.
73. Huber W, et al. Variance stabilization applied to microarray data calibration and to the quantification of differential expression. Bioinformatics. 2002;18(Suppl 1):S96-104.
74. Thurman TJ, et al. proteoDA: a package for quantitative proteomics. Journal of Open Source Software. 2023;8(85):5184.
75. Ge SX, Jung D, Yao R. ShinyGO: a graphical gene-set enrichment tool for animals and plants. Bioinformatics. 2020;36(8):2628–9.
76. Williams BB, Mundell N, Dunlap J, Jessen J. The planar cell polarity protein VANGL2 coordinates remodeling of the extracellular matrix. Commun Integr Biol. 2012;5(4):325–8.
77. New J, et al. Secretory Autophagy in Cancer-Associated Fibroblasts Promotes Head and Neck Cancer Progression and Offers a Novel Therapeutic Target. Cancer Res. 2017;77(23):6679–91.
78. Vélez-Bermúdez IC, et al. Protein and antibody purification followed by immunoprecipitation of MYB and GATA zinc finger-type maize proteins with magnetic beads. STAR Protocols. 2022;3(2): 101449.
79. Lagundžin D, Krieger KL, Law HC, Woods NT. An optimized co-immunoprecipitation protocol for the analysis of endogenous protein-protein interactions in cell lines using mass spectrometry. STAR Protoc. 2022;3(1): 101234.
80. Snipas SJ, et al. Gain of function of a metalloproteinase associated with multiple myeloma, bicuspid aortic valve, and Von Hippel-Lindau syndrome. Biochem J. 2022;479(14):1533–42.
81. Vandooren J, et al. Gelatin degradation assay reveals MMP-9 inhibitors and function of O-glycosylated domain. World J Biol Chem. 2011;2(1):14–24.
82. Gao, J., et al., Integrative analysis of complex cancer genomics and clinical profiles using the cBioPortal. Sci Signal, 2013. 6(269):pl1.
83. Cerami E, et al. The cBio Cancer Genomics Portal: An Open Platform for Exploring Multidimensional Cancer Genomics Data. Cancer Discov. 2012;2(5):401–4.
84. Abramson J, et al. Accurate structure prediction of biomolecular interactions with AlphaFold 3. Nature. 2024;630(8016):493–500.

Publisher's Note